Chandra Early-type Galaxy Atlas

Dong-Woo Kim[1] , Craig Anderson[1], Douglas Burke[1] , Raffaele D'Abrusco[1] , Giuseppina Fabbiano[1] , Antonella Fruscione[1],
Jennifer Lauer[1], Michael McCollough[1] , Douglas Morgan[1], Amy Mossman[1], Ewan O'Sullivan[1] , Alessandro Paggi[1] ,
Saeqa Vrtilek[1], and Ginevra Trinchieri[2]
[1] Center for Astrophysics|Harvard & Smithsonian 60 Garden Street, Cambridge, MA 02138, USA
[2] INAF-Osservatorio Astronomico di Brera, Via Brera 28, I-20121 Milan, Italy

Abstract

The hot interstellar medium (ISM) in early-type galaxies (ETGs) plays a crucial role in understanding their formation and evolution. The structural features of the hot gas identified by *Chandra* observations point to key evolutionary mechanisms, (e.g., active galactic nuclei, AGN, and stellar feedback, merging history). In our *Chandra* Galaxy Atlas (CGA) project, taking full advantage of the *Chandra* capabilities, we systematically analyzed the archival *Chandra* data of 70 ETGs and produced uniform data products for the hot gas properties. The primary data products are spatially resolved 2D spectral maps of the hot gas from individual galaxies. We emphasize that new features can be identified in the spectral maps that are not readily visible in the surface brightness maps. The high-level images can be viewed at the dedicated CGA website, and the CGA data products can be downloaded to compare with data at other wavelengths and to perform further analyses. Using our data products, we address a few focused science topics.

Key words: galaxies: elliptical and lenticular, cD – X-rays: galaxies

1. Introduction

For the past two decades, the *Chandra X-ray Observatory* has revolutionized many essential science subjects in astronomy and astrophysics. The main driving force is its unprecedentedly high spatial resolution[3]—the capability to resolve fine structures in a subarcsecond spatial scale. The study of the hot interstellar medium (ISM) in early-type galaxies (ETGs) can be taken to a new level thanks to this resolution. The hot ISM, which is the dominant phase in ETGs (e.g., see Kim & Pellegrini 2012), plays a crucial role in understanding the formation and evolution of the host galaxies. Various structural features of the hot ISM, which was previously considered as smooth and featureless, have been identified by *Chandra*. They include cavities, cold fronts, filaments, and tails, which are closely related to critical astrophysical mechanisms for the galaxy formation and evolution, e.g., AGN feedback, merging history, accretion, stripping, and star formation (SF) and its quenching (e.g., see Kim & Pellegrini 2012 and references therein).

Using the first four years of *Chandra* observations, Diehl & Statler (2007, 2008a, 2008b) assembled a sample of 54 nearby ($D \lesssim 100$ Mpc) ETGs (or 36 with temperature profiles). These authors produced a systematic characterization of the hot gas morphology and compared this morphology with the optical stellar distribution, radio emission, and AGN properties. Using the first 15 yr of *Chandra* observations, we have expanded the nearby ETG sample to 70 galaxies and produced spatially resolved homogeneous data products with additional spectral information. Previous archival studies have often focused on the global properties or 1D radial profiles (e.g., Kim & Fabbiano 2015; Lakhchaura et al. 2018). To explore the 2D distribution of spectral properties of the hot gas, we applied four different spatial binning techniques. In particular, the 2D spectral maps (of the hot gas temperature, normalized emission measure, projected pseudo-pressure, and projected pseudo-entropy) can reveal unique features that may not be visible in 1D radial profiles or the 2D surface brightness maps alone.

Although many galaxies were previously investigated, those studies were mostly done individually (see Appendix B). We provide uniformly reduced data products so that the entire sample of ETGs can be examined consistently. We also note that some *Chandra* data are extensively investigated for the first time as part of this project (e.g., NGC 1132 by Kim et al. 2018). We make use of new and improved data analysis (and statistical) techniques (e.g., CIAO[4] s/w package v4.9), instrument calibration data (in *Chandra* CALDB[5] v4.7), and atomic data (in ATOMDB[6] v3).

This paper is organized as follows. In Section 2 we describe the sample selection and observational information of each *Chandra* archival data. In Section 3 we describe the *Chandra* data analysis techniques and related issues. In Section 4 we present the data products of the *Chandra* Galaxy Atlas (CGA), our guidelines for general users on how to use the CGA data, and data caveats in the current version. In Section 5 we explain current and future focused science goals. In Appendix A we list the CGA data products (downloadable) and their descriptions in detail. In Appendix B we present the notes on individual galaxies. Throughout this paper, we quote errors at the 1σ significance level.

---

[3] http://cxc.harvard.edu/cdo/about_chandra/overview_cxo.html

[4] http://cxc.harvard.edu/ciao/
[5] http://cxc.harvard.edu/caldb/
[6] http://www.atomdb.org

2. Sample Selection and *Chandra* Observations

Our sample contains 70 E and S0 galaxies (type <0, based on RC3[7]) for which observations are available from the public *Chandra* archive (up to AO15). Because many giant galaxies are in galaxy groups/clusters in the RC3 catalog, our sample includes several examples of brightest group/cluster galaxies (BCGs). However, we exclude large groups/clusters by limiting T_{GAS} below $\sim$1.5 keV, because T_{GAS} is a good measure of the total mass of the system. About 80% of the sample galaxies have $T_{GAS} = 0.3$–1.0 keV.

We use both ACIS-I and ACIS-S *Chandra* observations,[8] but exclude observations with grating. We limit the minimum exposure time to 10 ks to exclude snapshot observations for AGN studies. In Table 1 we list our sample with the basic galaxy information (e.g., R.A., decl., distance, size, and *K*-band luminosity) and the total *Chandra* exposure time (see the footnotes below).

As multiple *Chandra* observations are often merged for a given galaxy, we assign a unique merge id, or mid in short (Column 12 in Table 1; Column 3 in Table 2) to each galaxy data set. If only one *Chandra* observation is used, the mid is the same as the *Chandra* observation ID (obsid).

For multiple observations, the mid consists of five digits, like an obsid. The first digit is 9, followed by two digits indicating the number of obsids used. The last two digits (usually "01") are unique serial numbers to separate different combinations of observation parameters (e.g., set of obsids and set of chips). The exposure time of this merged data set (Column 13 in Table 1) is determined by summing the LIVETIME of the chip where the galaxy center lies, after removing background flares that were determined for each chip of each obsid. See Section 3 for details on how we removed background flares.

In Table 2 we list the *Chandra* observational information for each obsid, grouped by galaxy. They include the observation date (Column 4), off-axis angle (OAA; in arcmininutes) of the galaxy center from the telescope aim point (Column 5), detectors indicating ACIS-I or ACIS-S (Column 6) and chips (ccdid) used in this study (Column 7), ccdid where the galaxy center lies (Column 8), effective exposure after removing background flares (see Section 3.1), and observation-specific notes on individual obsid (Column 10).

3. Data Analysis

Using the CIAO science threads[9] as a guide, we have developed our own analysis pipelines to apply robust data reduction methods in three main steps: (1) merging multiple observations and imaging diffuse emission after excluding point sources, (2) adaptively binning to determine optimal spectral extraction regions, and (3) extracting spectra from each spatial bin, fitting, and mapping spectral parameters.

3.1. Merging Multiple Observations

Because 45% of the galaxies were observed multiple times with a range of observing configurations (e.g., different CCDs, pointing, roll angle, and field of view), it is critical to properly combine all observations without losing coherency.

For ACIS-I observations, we use the four front-illuminated chips I0-I3 (CCDID = 0–3), while for ACIS-S, we use the back-illuminated chip S3 (CCDID = 7), where the target lies, and the front-illuminated chip S2 (CCDID = 6), where the extended diffuse emission is often visible. Because the point-spread function (PSF)[10] becomes large at large OAAs, the other chips are generally not useful for our purposes. However, for a few special cases, we use a nonstandard set of chips (see Table 2). Similarly, we do not use observations where the target galaxy is at a large OAA (typically OAA > 4 arcmin) because of the large PSF.

Figure 1(a) illustrates an example of merging six (two ACIS-I and four ACIS-S) *Chandra* observations of NGC 1399. Figure 1(b) shows the DSS[11] optical image of the same region of the sky. In all observations, the center of NGC 1399 is within 1.5 arcmin from the aim point.

Figure 2 shows the entire data processing workflow. Once ACIS data are downloaded from the *Chandra* archive, we run the ACIS level 2 processing using the CIAO tool *chandra_repro*.[12] This step ensures that the most recent calibration data (e.g., CTI correction, time-dependent ACIS gain, bad pixels) are applied. To correct the relative positional error among multiple observations, we detect point sources from individual observations using the CIAO tool *wavdetect* (with scale = 1, 2, 4, 8 and sigthresh = 10^{-6}) in a *C*-band image (0.5–5 keV, see Table 3 for the definitions of energy bands used in CGA) made with the CIAO tool *fluximage*. Note that we run *fluximage* again after removing point sources detected on the merged data in Section 3.2. Then, we register bright (net counts > 30) point sources commonly detected in a pair of observations, using the CIAO tool *reproject_aspect* (with radius = 2 and residlim = 1). This positional correction is usually small (ΔR.A. and Δdecl. < $0\rlap{.}''5$) but necessary for the *Chandra* observations with a high spatial resolution. We rerun *chandra_repro* for the second time to apply the newly determined aspect solutions.

To remove the time intervals of background flares,[13] we generate light curves from the point-source removed event files, determine the mean rate and its standard deviation, then apply a CIAO tool *deflare* with 2σ clipping (see Markevitch's note[14] for more details about the ACIS background). While this method works for most observations, it fails in extreme cases when the flare occurs during a significant fraction of a given observation or the background rate changes gradually throughout the observation. We examine each light curve and manually remove the time interval with flares before determining the mean rate and standard deviation and rerun *deflare*. Background flares have varying effects on different chips, hence we apply this step to each CCD for a given observation.

To reproject individual observations onto a single tangent plane, we use the CIAO tool *reproject_obs*. To make merged images in multiple energy bands (before and after exposure correction), we use the CIAO tool *flux_obs*. Figure 1(c) shows an example of the merged *Chandra* observations of NGC 1399.

Table 1
CGA Sample

Name	R.A. (h m s)	Decl. (d m s)	D (Mpc)	Type	r_maj (arcmin)	r_min (arcmin)	PA (deg)	Re (arcmin)	log(L_K) log($L_\odot$)	N_H (10^{20} cm^{-2})	mid	exp (ks)
(1)	(2)	(3)	(4)	(5)	(6)	(7)	(8)	(9)	(10)	(11)	(12)	(13)
I1262	17 33 2.0	+43 45 34.6	130.0	−5.0	0.60	0.32	80.0	0.20	11.42	2.43	90401	138.8
I1459	22 57 10.6	−36 27 44.0	29.2	−5.0	2.62	1.90	42.5	0.62	11.54	1.17	02196	52.5
I1860	02 49 33.7	−31 11 21.0	93.8	−5.0	0.87	0.60	6.4	0.31	11.57	2.05	10537	36.8
I4296	13 36 39.0	−33 57 57.2	50.8	−5.0	1.69	1.62	45.0	0.80	11.74	4.09	03394	24.3
N0193	00 39 18.6	+03 19 52.0	47.0	−2.5	0.72	0.60	70.0	0.32	10.99	2.79	90201	106.7
N0315	00 57 48.9	+30 21 8.8	69.8	−4.0	1.62	1.02	45.0	0.62	11.84	5.92	90201	55.9
N0383	01 07 24.9	+32 24 45.0	63.4	−3.0	0.79	0.71	25.0	0.34	11.54	5.41	02147	42.9
N0499	01 23 11.5	+33 27 38.0	54.5	−2.5	0.81	0.64	70.0	0.28	11.31	5.21	90401	37.4
N0507	01 23 40.0	+33 15 20.0	63.8	−2.0	1.55	1.55	60.0	0.69	11.62	5.23	90201	60.3
N0533	01 25 31.4	+01 45 32.8	76.9	−5.0	1.90	1.17	47.5	0.72	11.73	3.07	02880	35.3
N0720	01 53 0.5	−13 44 19.2	27.7	−5.0	2.34	1.20	140.0	0.60	11.31	1.58	90401	92.4
N0741	01 56 21.0	+05 37 44.0	70.9	−5.0	1.48	1.44	90.0	0.64	11.72	4.44	02223	29.1
N1052	02 41 4.8	−08 15 20.8	19.4	−5.0	1.51	1.04	120.0	0.56	10.93	3.07	05910	57.2
N1132	02 52 51.8	−01 16 28.8	95.0	−4.5	1.26	0.67	150.0	0.56	11.58	5.19	90201	38.3
N1316	03 22 41.7	−37 12 29.6	21.5	−2.0	6.01	4.26	47.5	1.22	11.76	2.13	02022	23.6
N1332	03 26 17.3	−21 20 7.3	22.9	−3.0	2.34	0.72	112.5	0.46	11.23	2.30	90201	53.7
N1380	03 36 27.9	−34 58 32.9	17.6	−2.0	2.39	1.15	7.0	0.63	11.08	1.42	09526	37.0
N1387	03 36 57.1	−35 30 23.9	20.3	−3.0	1.41	1.41	110.0	0.59	10.98	14.50	04168	45.4
N1395	03 38 29.8	−23 01 39.7	24.1	−5.0	2.94	2.23	92.5	0.78	11.34	1.94	00799	16.4
N1399	03 38 29.1	−35 27 2.7	19.9	−5.0	3.46	3.23	150.0	0.81	11.41	1.49	90602	206.8
N1400	03 39 30.8	−18 41 17.0	26.4	−3.0	1.15	1.00	94.0	0.38	11.05	5.17	90202	54.6
N1404	03 38 51.9	−35 35 39.8	21.0	−5.0	1.66	1.48	162.5	0.45	11.25	1.51	91101	486.3
N1407	03 40 11.9	−18 34 48.4	28.8	−5.0	2.29	2.13	60.0	1.06	11.57	5.42	00791	41.9
N1550	04 19 37.9	+02 24 35.7	51.1	−3.2	1.12	0.97	30.0	0.43	11.24	11.25	90401	106.8
N1553	04 16 10.5	−55 46 48.5	18.5	−2.0	2.23	1.41	150.0	0.95	11.36	1.49	00783	16.6
N1600	04 31 39.9	−05 05 10.0	57.4	−5.0	1.23	0.83	5.0	0.81	11.63	4.86	90201	48.7
N1700	04 56 56.3	−04 51 56.7	44.3	−5.0	1.66	1.04	85.0	0.30	11.39	4.76	02069	29.5
N2300	07 32 20.0	+85 42 34.2	30.4	−2.0	1.41	1.02	108.0	0.55	11.25	5.49	90201	65.7
N2563	08 20 35.7	+21 04 4.0	67.8	−2.0	1.04	0.76	70.0	0.32	11.39	4.25	07925	48.1
N3115	10 05 14.0	−07 43 6.9	9.7	−3.0	3.62	1.23	45.0	0.57	10.95	4.61	91101	1088.5
N3379	10 47 49.6	+12 34 53.9	10.6	−5.0	2.69	2.39	67.5	0.78	10.87	2.78	90501	325.2
N3402	10 50 26.1	−12 50 42.3	64.9	−4.0	1.04	1.04	170.0	0.47	11.39	4.50	03243	28.0
N3607	11 16 54.6	+18 03 7.0	22.8	−2.0	2.45	1.23	125.0	0.76	11.25	1.48	02073	38.5
N3608	11 16 59.0	+18 08 55.3	22.9	−5.0	1.58	1.29	80.0	0.49	10.81	1.48	02073	37.7
N3842	11 44 2.1	+19 56 59.0	97.0	−5.0	0.71	0.51	175.0	0.63	11.67	2.27	04189	42.4
N3923	11 51 1.8	−28 48 22.0	22.9	−5.0	2.94	1.95	47.5	0.88	11.45	6.30	90201	94.5
N4104	12 06 39.0	+28 10 27.1	120.0	−2.0	1.29	0.77	35.0	0.57	11.89	1.67	06939	33.8
N4125	12 08 6.0	+65 10 26.9	23.9	−5.0	2.88	1.58	82.5	0.85	11.35	1.82	02071	60.6
N4261	12 19 23.2	+05 49 30.8	31.6	−5.0	2.04	1.82	172.5	0.75	11.43	1.58	90201	130.3
N4278	12 20 6.8	+29 16 50.7	16.1	−5.0	2.04	1.90	27.5	0.56	10.87	1.76	90901	557.6
N4291	12 20 17.8	+75 22 14.8	26.2	−5.0	0.95	0.79	110.0	0.27	10.80	2.88	11778	28.2
N4325	12 23 6.7	+10 37 16.0	110.0	0.0	0.48	0.32	175.0	0.33	11.29	2.14	03232	28.0
N4342	12 23 39.0	+07 03 14.4	16.5	−3.0	0.64	0.30	165.0	0.10	10.16	1.60	90201	74.4
N4374	12 25 3.7	+12 53 13.1	18.4	−5.0	3.23	2.81	122.5	1.02	11.37	2.78	90301	112.4
N4382	12 25 24.1	+18 11 27.9	18.4	−1.0	3.54	2.75	12.5	1.38	11.41	2.50	02016	38.2
N4406	12 26 11.7	+12 56 46.0	17.1	−5.0	4.46	2.88	125.0	2.07	11.36	2.69	90202	22.0
N4438	12 27 45.6	+13 00 31.8	18.0	0.0	4.26	1.58	20.5	0.95	10.94	2.60	90201	25.0
N4472	12 29 46.8	+08 00 1.7	16.3	−5.0	5.12	4.16	162.5	1.74	11.60	1.62	90501	362.5
N4477	12 30 2.2	+13 38 11.8	16.5	−2.0	1.90	1.73	40.0	0.73	10.83	2.65	90401	117.4
N4526	12 34 3.0	+07 41 56.9	16.9	−2.0	3.62	1.20	113.0	0.68	11.20	1.63	03925	36.1
N4552	12 35 39.8	+12 33 22.8	15.3	−5.0	2.56	2.34	150.0	0.68	11.01	2.56	90401	197.0
N4555	12 35 41.2	+26 31 23.0	91.5	−5.0	0.95	0.81	120.0	0.50	11.59	1.33	02884	26.4
N4594	12 39 59.4	−11 37 23.0	9.8	1.0	4.35	1.77	87.5	1.19	11.33	3.67	90301	186.7
N4636	12 42 49.9	+02 41 16.0	14.7	−5.0	3.01	2.34	142.5	1.56	11.10	1.82	90401	191.1
N4649	12 43 40.0	+11 33 9.7	16.8	−5.0	3.71	3.01	107.5	1.28	11.49	2.13	90601	284.2
N4782	12 54 35.7	−12 34 7.1	60.0	−5.0	0.89	0.85	5.0	0.25	11.79	3.58	03220	48.3
N5044	13 15 24.0	−16 23 7.9	31.2	−5.0	1.48	1.48	10.0	0.42	11.24	4.94	90201	102.1
N5129	13 24 10.0	+13 58 36.0	103.0	−5.0	0.85	0.71	5.0	0.48	11.66	1.76	90201	43.2
N5171	13 29 21.5	+11 44 6.0	100.0	−3.0	0.55	0.41	0.0	0.43	11.32	1.94	03216	34.4
N5813	15 01 11.3	+01 42 7.1	32.2	−5.0	2.08	1.51	130.0	0.89	11.38	4.25	90901	616.8
N5846	15 06 29.3	+01 36 20.2	24.9	−5.0	2.04	1.90	27.5	0.99	11.34	4.24	90201	109.4
N5866	15 06 29.5	+55 45 47.6	15.3	−1.0	2.34	0.97	123.0	0.64	10.96	1.47	02879	30.7

Table 1
(Continued)

Name	R.A. (h m s)	Decl. (d m s)	D (Mpc)	Type	r_maj (arcmin)	r_min (arcmin)	PA (deg)	Re (arcmin)	log(L_K) log($L_\odot$)	N_H (10^{20} cm^{-2})	mid	exp (ks)
(1)	(2)	(3)	(4)	(5)	(6)	(7)	(8)	(9)	(10)	(11)	(12)	(13)
N6107	16 17 20.1	+34 54 5.0	127.9	−5.0	0.43	0.33	27.5	0.44	11.79	1.49	08180	18.7
N6338	17 15 23.0	+57 24 40.0	123.0	−2.0	0.76	0.51	15.0	0.48	11.75	2.60	04194	46.6
N6482	17 51 48.8	+23 04 19.0	58.4	−5.0	1.00	0.85	65.0	0.37	11.52	7.77	03218	16.4
N6861	20 07 19.4	−48 22 11.5	28.1	−3.0	1.41	0.91	140.0	0.38	11.14	5.01	90201	110.1
N6868	20 09 54.1	−48 22 46.0	26.8	−5.0	1.77	1.41	80.0	0.50	11.26	4.96	90201	94.5
N7618	23 19 47.2	+42 51 9.5	74.0	−5.0	0.60	0.50	10.0	0.36	11.46	11.93	90301	75.2
N7619	23 20 14.5	+08 12 22.5	53.0	−5.0	1.26	1.15	40.0	0.57	11.57	5.04	90201	55.0
N7626	23 20 42.5	+08 13 1.0	56.0	−5.0	1.32	1.17	10.0	0.74	11.62	5.05	02074	26.2

Note. Column 1. Galaxy name (NGC or IC name). Columns 2–3. R.A. and decl. (J2000) from 2MASS via NED (http://ned.ipac.caltech.edu). Column 4. Distance in megaparsec, primarily taken from Tonry et al. (2001), Cappellari et al. (2011), and Tully et al. (2013). If not listed in the above references, we take a mean value from NED. Column 5. Type taken from RC3. Columns 6–7. Semimajor and semiminor axis of the D_{25} ellipse in arcminutes taken from RC3. Column 8. Position angle of the D_{25} ellipse from 2MASS via NED, measured eastward from the north. Column 9. Effective radius in arcmin taken from RC3. Column 10. K-band luminosity from 2MASS (K_tot mag) via NED (assuming M_K(Sun) = 3.28 mag and D in column 4). Column 11. Galactic line-of-sight column hydrogen density in units of 10^{20} cm^{-2} by colden (http://asc.harvard.edu/toolkit/colden.jsp). Column 12. The *Chandra* merge id (mid in short—see Table 2 for individual obsids). Column 13. The total effective exposure in ks (see Table 2 for the exposures for individual obsids).

3.2. Point-source Detection and Removal

We run *wavdetect* for the second time to detect point sources from the merged images in multiple energy bands. To remove point sources, we primarily use the point sources detected in the C band (0.5–5 keV). We have experimented with various energy bands and conclude that adding lower or higher energies (below 0.5 keV and above 5 keV) does not result in more secure or a greater number of detections because we include more background than source signal and therefore actually reduce the signal-to-noise ratio (S/N).

Because our goal is to investigate the diffuse emission, we do not remove the faint (possibly false) sources and remove only real sources by applying net counts >10 and S/N > 3. We discuss the point-source properties including faint sources in a separate paper.

To determine the size of each point source, we simulate the PSF for each source for each observation, using MARX.[15] We have compared MARX-PSFs with those made by more accurate ray tracing (SAO-Trace) and found no significant difference for our purpose. We reproject the simulated PSF onto the same tangent plane as the observation and merge them to produce an exposure-weighted mean PSF image as in the merged real observations. We apply variable encircled energy (EE) fractions from 90% to 98%, depending on the net counts to optimally remove photons from point sources (see Table 4), i.e., higher fractions for brighter sources so that we can effectively remove the wing of a bright source, but lower fractions for faint sources to remove only the PSF core.

Near the galaxy center where the hot gas emission peaks, *wavdetect* may detect false sources or miss real sources, and the source positions may be uncertain. These problems are particularly severe in systems with narrow, high surface brightness gas substructures (e.g., in NGC 4374 and NGC 4636). Instead of the C band, we use the wavdetect sources detected in the H band (2–7 keV), as the point sources (mostly LMXBs and background AGNs) are expected to have a harder spectrum than the hot gas (e.g., Boroson et al. 2011). We empirically determined the optimal radius inside which we use

the H band (rather than the C band) by examining several galaxies with complex hot gas structures. We found this radius where the count in one ACIS pixel in the C band is 1. In Figure 3 we compare the point sources detected in the C band and H band in the central region of NGC 4374. The two sources detected only in C band are marked by the red arrows. As they are likely hot gas blobs, we do not exclude them as X-ray binaries. Another two sources with uncertain positions and sizes (in C band) are marked by the black arrows. We use the H-band positions and PSF-based source sizes for them.

To make diffuse gas images, we refill the point-source elliptical regions with values interpolated from surrounding pixels[16] by using a series of CIAO tools, *roi*, *splitroi*, and *dmfilth*. Then, we generate point-source-excluded, refilled, exposure-corrected images with the CIAO tool *fluximage* and smoothed images with the CIAO tool *aconvolve*. Figure 1(d) shows an example of the diffuse emission of NGC 1399.

We note that while we use the merged data to detect point sources and to perform spatial binning (see Section 3.3), we analyze the individual observations for extracting the X-ray spectra and producing the corresponding calibration files, rmf/arf (see Section 3.4), because the CCD responses and PSFs vary as a function of detector location, photon energy, and observing time.

When a central AGN is very bright (count rate $\gtrsim 0.1$ per second), its ACIS observation suffers from a readout streak problem.[17] We determine the streak region by *acis_streak_map* for each observation and remove the region from individual event files for the adaptive binning and spectral analysis (Sections 3.3–3.5), and we also remove the point sources (see the related issue in Section 4.3).

3.3. Adaptive Binning

The most innovative step in our CGA project is to apply four adaptive binning methods to characterize the 2D spatial/spectral properties of the hot gas.

---

[15] http://space.mit.edu/cxc/marx/

[16] http://cxc.harvard.edu/ciao/threads/diffuse_emission/index.html#bkgreg
[17] http://cxc.harvard.edu/ciao/threads/acisreadcorr/

Table 2
Chandra Observations

obsid	Name	mid	obs_date year month day	OAA (arcmin)	Detector	CCDid	Target CCD	eff_exp (ks)	Notes
(1)	(2)	(3)	(4)	(5)	(6)	(7)	(8)	(9)	(10)
02018	I1262	90401	2001 Aug 23	0.2	ACIS-S	6, 7	7	28.7	
06949	I1262	90401	2006 Apr 17	0.0	ACIS-I	0, 1, 2, 3	3	38.6	
07321	I1262	90401	2006 Apr 19	0.0	ACIS-I	0, 1, 2, 3	3	35.0	
07322	I1262	90401	2006 Apr 22	0.0	ACIS-I	0, 1, 2, 3	3	36.5	
02196	I1459	02196	2001 Aug 12	0.0	ACIS-S	6, 7	7	52.5	a c
10537	I1860	10537	2009 Sep 12	0.0	ACIS-S	6, 7	7	36.8	
03394	I4296	03394	2001 Dec 15	0.1	ACIS-S	6, 7	7	24.3	a
04053	N0193	90201	2003 Sep 1	0.0	ACIS-S	6, 7	7	16.6	
11389	N0193	90201	2009 Aug 21	0.0	ACIS-S	6, 7	7	90.1	
04156	N0315	90201	2003 Feb 22	0.0	ACIS-S	6, 7	7	51.2	a c
00855	N0315	90201	2000 Oct 8	0.0	ACIS-S	7	7	4.7	b c
02147	N0383	02147	2000 Nov 6	0.0	ACIS-S	6, 7	7	42.9	
10536	N0499	90401	2009 Feb 12	0.0	ACIS-S	6, 7	7	18.4	
10865	N0499	90401	2009 Feb 4	0.0	ACIS-S	6, 7	7	4.4	
10866	N0499	90401	2009 Feb 5	0.0	ACIS-S	6, 7	7	7.8	
10867	N0499	90401	2009 Feb 7	0.0	ACIS-S	6, 7	7	6.8	
00317	N0507	90201	2000 Oct 11	0.2	ACIS-S	6, 7	7	17.7	
02882	N0507	90201	2002 Jan 8	0.4	ACIS-I	0, 1, 2, 3	3	42.6	
02880	N0533	02880	2002 Jul 28	0.0	ACIS-S	6, 7	7	35.3	
07062	N0720	90401	2006 Oct 9	0.0	ACIS-S	6, 7	7	20.2	
07372	N0720	90401	2006 Aug 6	0.0	ACIS-S	6, 7	7	46.3	
08448	N0720	90401	2006 Oct 12	0.0	ACIS-S	6, 7	7	7.5	
08449	N0720	90401	2006 Oct 12	0.0	ACIS-S	6, 7	7	18.4	
02223	N0741	02223	2001 Jan 28	0.0	ACIS-S	6, 7	7	29.1	
05910	N1052	05910	2005 Sep 18	0.0	ACIS-S	6, 7	7	57.2	
00801	N1132	90201	1999 Dec 10	0.1	ACIS-S	6, 7	7	11.7	
03576	N1132	90201	2003 Nov 16	0.0	ACIS-S	6, 7	7	26.6	
02022	N1316	02022	2001 Apr 17	0.0	ACIS-S	6, 7	7	23.6	
02915	N1332	90201	2002 Sep 18	0.1	ACIS-S	6, 7	7	4.6	
04372	N1332	90201	2002 Sep 19	0.1	ACIS-S	6, 7	7	49.1	
09526	N1380	09526	2008 Mar 26	0.1	ACIS-S	6, 7	7	37.0	
04168	N1387	04168	2003 May 20	0.9	ACIS-I	0, 1, 2, 3	3	45.4	
00799	N1395	00799	1999 Dec 31	0.0	ACIS-I	0, 1, 2, 3	3	16.4	
00239	N1399	90602	2000 Jan 19	0.1	ACIS-I	0, 1, 2, 3	3	3.6	
00319	N1399	90602	2000 Jan 18	0.1	ACIS-S	6, 7	7	51.9	
04172	N1399	90602	2003 May 26	1.5	ACIS-I	0, 1, 2, 3	3	41.4	
09530	N1399	90602	2008 Jun 8	0.0	ACIS-S	6, 7	7	56.5	
14527	N1399	90602	2013 Jul 1	0.0	ACIS-S	6, 7	7	24.5	
16639	N1399	90602	2014 Oct 12	0.0	ACIS-S	6, 7	7	28.9	
14033	N1400	90202	2012 Jun 17	2.7	ACIS-S	7	7	49.7	
07849	N1400	90202	2007 Jul 11	0.0	ACIS-S	6, 7	7	4.9	
02942	N1404	91101	2003 Feb 13	0.1	ACIS-S	6, 7	7	28.2	
04174	N1404	91101	2003 May 28	1.2	ACIS-I	0, 1, 2, 3	3	43.6	
09798	N1404	91101	2007 Dec 24	1.2	ACIS-S	6, 7	7	18.2	
09799	N1404	91101	2007 Dec 27	1.2	ACIS-S	6, 7	7	16.4	
16231	N1404	91101	2014 Oct 20	1.9	ACIS-S	6, 7	7	57.9	
16232	N1404	91101	2014 Nov 12	2.5	ACIS-S	6, 7	7	67.6	
16233	N1404	91101	2014 Nov 9	2.5	ACIS-S	6, 7	7	95.7	
17540	N1404	91101	2014 Nov 2	1.9	ACIS-S	6, 7	7	28.1	
17541	N1404	91101	2014 Oct 23	1.9	ACIS-S	6, 7	7	23.7	
17548	N1404	91101	2014 Nov 11	2.5	ACIS-S	6, 7	7	47.5	
17549	N1404	91101	2015 Mar 28	2.7	ACIS-S	6, 7	7	59.4	
00791	N1407	00791	2000 Aug 16	0.0	ACIS-S	6, 7	7	41.9	
03186	N1550	90401	2002 Jan 8	0.9	ACIS-I	0, 1, 2, 3	3	10.0	
03187	N1550	90401	2002 Jan 8	0.9	ACIS-I	0, 1, 2, 3	1	9.6	
05800	N1550	90401	2005 Oct 22	4.0	ACIS-S	6, 7	7	44.3	
05801	N1550	90401	2005 Oct 24	4.1	ACIS-S	6, 7	7	42.9	
00783	N1553	00783	2000 Jan 2	0.0	ACIS-S	6, 7	7	16.6	
04283	N1600	90201	2002 Sep 18	0.0	ACIS-S	6, 7	7	21.9	
04371	N1600	90201	2002 Sep 20	0.0	ACIS-S	6, 7	7	26.8	
02069	N1700	02069	2000 Nov 3	0.1	ACIS-S	6, 7	7	29.5	
04968	N2300	90201	2004 Jun 23	6.6	ACIS-S	6, 7	6	44.5	

Table 2
(Continued)

obsid	Name	mid	obs_date year month day	OAA (arcmin)	Detector	CCDid	Target CCD	eff_exp (ks)	Notes
(1)	(2)	(3)	(4)	(5)	(6)	(7)	(8)	(9)	(10)
15648	N2300	90201	2013 May 24	7.0	ACIS-S	6, 7	6	21.2	
07925	N2563	07925	2007 Sep 18	2.9	ACIS-I	0, 1, 2, 3	1	48.1	
13820	N3115	91101	2012 Jan 31	0.0	ACIS-S	6, 7	7	179.1	
02040	N3115	91101	2001 Jun 14	0.1	ACIS-S	6, 7	7	33.5	
11268	N3115	91101	2010 Jan 27	0.0	ACIS-S	6, 7	7	40.1	
12095	N3115	91101	2010 Jan 29	0.0	ACIS-S	6, 7	7	74.1	
13817	N3115	91101	2012 Jan 18	0.0	ACIS-S	6, 7	7	166.3	
13819	N3115	91101	2012 Jan 26	0.0	ACIS-S	6, 7	7	68.6	
13821	N3115	91101	2012 Feb 3	0.0	ACIS-S	6, 7	7	151.1	
13822	N3115	91101	2012 Jan 21	0.0	ACIS-S	6, 7	7	148.4	
14383	N3115	91101	2012 Apr 4	0.0	ACIS-S	6, 7	7	117.4	
14384	N3115	91101	2012 Apr 6	0.0	ACIS-S	6, 7	7	67.4	
14419	N3115	91101	2012 Apr 5	0.0	ACIS-S	6, 7	7	42.5	
01587	N3379	90501	2001 Feb 13	0.1	ACIS-S	6, 7	7	30.5	
07073	N3379	90501	2006 Jan 23	0.0	ACIS-S	6, 7	7	82.3	
07074	N3379	90501	2006 Apr 9	0.0	ACIS-S	6, 7	7	68.3	
07075	N3379	90501	2006 Jul 3	0.0	ACIS-S	6, 7	7	80.0	
07076	N3379	90501	2007 Jan 10	0.0	ACIS-S	6, 7	7	64.1	
03243	N3402	03243	2002 Nov 5	0.3	ACIS-S	6, 7	7	28.0	
02073	N3607	02073	2001 Jun 12	3.6	ACIS-I	0, 1, 2, 3	2	38.5	
02073	N3608	02073	2001 Jun 12	2.3	ACIS-I	0, 1, 2, 3	3	37.7	
04189	N3842	04189	2003 Jan 24	1.8	ACIS-S	6, 7	7	42.4	
01563	N3923	90201	2001 Jun 14	0.1	ACIS-S	6, 7	7	15.7	
09507	N3923	90201	2008 Apr 11	0.1	ACIS-S	6, 7	7	78.8	
06939	N4104	06939	2006 Feb 16	0.7	ACIS-S	6, 7	7	33.8	
02071	N4125	02071	2001 Sep 9	0.1	ACIS-S	6, 7	7	60.6	
09569	N4261	90201	2008 Feb 12	0.1	ACIS-S	6, 7	7	97.9	
00834	N4261	90201	2000 May 6	0.0	ACIS-S	6, 7	7	32.4	a
07077	N4278	90901	2006 Mar 16	0.0	ACIS-S	7	7	104.4	
00398	N4278	90901	2000 Apr 20	0.0	ACIS-S	7	7	1.2	a
04741	N4278	90901	2005 Feb 3	0.0	ACIS-S	7	7	35.4	
07078	N4278	90901	2006 Jul 25	0.0	ACIS-S	7	7	49.1	
07079	N4278	90901	2006 Oct 24	0.0	ACIS-S	7	7	99.8	
07080	N4278	90901	2007 Apr 20	0.0	ACIS-S	7	7	55.6	
07081	N4278	90901	2007 Feb 20	0.0	ACIS-S	7	7	108.2	
11269	N4278	90901	2010 Mar 15	0.0	ACIS-S	7	7	79.1	
12124	N4278	90901	2010 Mar 20	0.0	ACIS-S	7	7	24.8	
11778	N4291	11778	2010 Dec 11	0.0	ACIS-S	6, 7	7	28.2	
03232	N4325	03232	2003 Feb 4	0.0	ACIS-S	6, 7	7	28.0	
04687	N4342	90201	2005 Feb 11	0.0	ACIS-S	6, 7	7	30.3	
12955	N4342	90201	2011 Feb 17	0.0	ACIS-S	6, 7	7	44.1	
05908	N4374	90301	2005 May 1	0.0	ACIS-S	6, 7	7	45.1	
06131	N4374	90301	2005 Nov 7	0.0	ACIS-S	6, 7	7	39.1	
00803	N4374	90301	2000 May 19	0.0	ACIS-S	6, 7	7	28.2	
02016	N4382	02016	2001 May 29	0.1	ACIS-S	6, 7	7	38.2	
00318	N4406	90202	2000 Apr 7	0.2	ACIS-S	2, 3, 6, 7	7	10.2	
00963	N4406	90202	2000 Apr 7	0.2	ACIS-S	2, 3, 6, 7	7	11.8	d
02883	N4438	90201	2002 Jan 29	0.0	ACIS-S	6, 7	7	21.2	
08042	N4438	90201	2008 Feb 11	4.4	ACIS-S	6, 7	7	3.8	
00321	N4472	90501	2000 Jun 12	0.2	ACIS-S	6, 7	7	27.8	
00322	N4472	90501	2000 Mar 19	0.2	ACIS-I	0, 1, 2, 3	3	10.4	
11274	N4472	90501	2010 Feb 27	0.0	ACIS-S	6, 7	7	37.6	
12888	N4472	90501	2011 Feb 21	0.0	ACIS-S	6, 7	7	155.7	
12889	N4472	90501	2011 Feb 14	0.0	ACIS-S	6, 7	7	131.0	
08066	N4477	90401	2008 Feb 21	5.3	ACIS-S	6, 7	6	4.8	
09527	N4477	90401	2008 Apr 27	0.0	ACIS-S	6, 7	7	36.4	
11736	N4477	90401	2010 Apr 30	3.7	ACIS-S	6, 7	6	56.3	
12209	N4477	90401	2010 May 2	3.7	ACIS-S	6, 7	6	19.9	
03925	N4526	03925	2003 Nov 14	0.0	ACIS-S	6, 7	7	36.1	
02072	N4552	90401	2001 Apr 22	0.0	ACIS-S	6, 7	7	52.1	
13985	N4552	90401	2012 Apr 22	0.0	ACIS-S	6, 7	7	49.4	
14358	N4552	90401	2012 Aug 10	1.2	ACIS-S	6, 7	7	48.9	

Table 2
(Continued)

obsid	Name	mid	obs_date year month day	OAA (arcmin)	Detector	CCDid	Target CCD	eff_exp (ks)	Notes
(1)	(2)	(3)	(4)	(5)	(6)	(7)	(8)	(9)	(10)
14359	N4552	90401	2012 Apr 23	1.0	ACIS-S	6, 7	7	46.6	
02884	N4555	02884	2003 Feb 4	0.0	ACIS-S	6, 7	7	26.4	
09532	N4594	90301	2008 Apr 29	0.5	ACIS-I	0, 1, 2, 3	3	83.6	
09533	N4594	90301	2008 Dec 2	0.0	ACIS-I	0, 1, 2, 3	3	85.6	
01586	N4594	90301	2001 May 31	0.1	ACIS-S	6, 7	7	17.5	
00323	N4636	90401	2000 Jan 26	0.0	ACIS-S	6, 7	7	42.4	
00324	N4636	90401	1999 Dec 4	0.0	ACIS-I	0, 1, 2, 3	3	5.5	
03926	N4636	90401	2003 Feb 14	0.0	ACIS-I	0, 1, 2, 3	3	71.4	
04415	N4636	90401	2003 Feb 15	0.0	ACIS-I	0, 1, 2, 3	3	71.8	
14328	N4649	90601	2011 Aug 12	0.1	ACIS-S	6, 7	7	14.0	
12975	N4649	90601	2011 Aug 8	0.1	ACIS-S	6, 7	7	83.1	
12976	N4649	90601	2011 Feb 24	0.1	ACIS-S	6, 7	7	99.0	
00785	N4649	90601	2000 Apr 20	0.2	ACIS-S	6, 7	7	23.0	
08182	N4649	90601	2007 Jan 30	0.1	ACIS-S	6, 7	7	47.8	
08507	N4649	90601	2007 Feb 1	0.1	ACIS-S	6, 7	7	17.3	
03220	N4782	03220	2002 Jun 16	0.3	ACIS-S	6, 7	7	48.3	
00798	N5044	90201	2000 Mar 19	0.0	ACIS-S	6, 7	7	20.2	
09399	N5044	90201	2008 Mar 7	0.0	ACIS-S	6, 7	7	81.9	
06944	N5129	90201	2006 Apr 13	0.5	ACIS-S	6, 7	7	19.9	
07325	N5129	90201	2006 May 14	0.5	ACIS-S	6, 7	7	23.3	
03216	N5171	03216	2002 Dec 10	0.9	ACIS-S	6, 7	7	34.4	
05907	N5813	90901	2005 Apr 2	0.0	ACIS-S	7	7	46.8	
09517	N5813	90901	2008 Jun 5	1.5	ACIS-S	7	7	97.5	
12951	N5813	90901	2011 Mar 28	2.5	ACIS-S	7	7	71.4	
12952	N5813	90901	2011 Apr 5	2.5	ACIS-S	7	7	141.8	
12953	N5813	90901	2011 Apr 7	2.5	ACIS-S	7	7	30.0	
13246	N5813	90901	2011 Mar 30	2.5	ACIS-S	7	7	40.4	
13247	N5813	90901	2011 Mar 31	2.5	ACIS-S	7	7	33.2	
13253	N5813	90901	2011 Apr 8	2.5	ACIS-S	7	7	114.9	
13255	N5813	90901	2011 Apr 10	2.5	ACIS-S	7	7	40.8	
07923	N5846	90201	2007 Jun 12	0.0	ACIS-I	0, 1, 2, 3	3	86.2	
00788	N5846	90201	2000 May 24	0.1	ACIS-S	6, 7	7	23.2	
02879	N5866	02879	2002 Nov 14	0.0	ACIS-S	6, 7	7	30.7	
08180	N6107	08180	2007 Sep 29	0.1	ACIS-S	6, 7	7	18.7	
04194	N6338	04194	2003 Sep 17	0.0	ACIS-I	0, 1, 2, 3	3	46.6	
03218	N6482	03218	2002 May 20	0.0	ACIS-S	6, 7	7	16.4	
03190	N6861	90201	2002 Jul 26	0.1	ACIS-I	0, 1, 2, 3	1	18.9	
11752	N6861	90201	2009 Aug 13	0.0	ACIS-I	0, 1, 2, 3	3	91.2	
03191	N6868	90201	2002 Nov 1	0.0	ACIS-I	0, 1, 2, 3	2	22.4	
11753	N6868	90201	2009 Aug 19	0.0	ACIS-I	0, 1, 2, 3	3	72.1	
00802	N7618	90301	1999 Dec 10	0.0	ACIS-S	6, 7	7	10.5	
07895	N7618	90301	2007 Sep 8	0.0	ACIS-S	6, 7	7	34.0	
16014	N7618	90301	2014 Sep 10	1.4	ACIS-S	6, 7	7	30.7	
03955	N7619	90201	2003 Sep 24	3.6	ACIS-S	6, 7	7	29.0	
02074	N7619	90201	2001 Aug 20	2.6	ACIS-I	0, 1, 2, 3	2	26.0	
02074	N7626	02074	2001 Aug 20	5.8	ACIS-I	0, 1, 2, 3	1	26.2	

Note. Column 1. Unique *Chandra* observation identification number. Column 2. Galaxy name (NGC or IC name). Column 3. The merge id (mid in short) is an identification number when data from multiple obsids are used. Column 4. Observation date. Column 5. OAA (off-axis-angle) of the galaxy center in arcminutes. Column 6. Detector (ACIS-I or ACIS-S). Column 7. Chips used in CGA. Column 8. The chip where the center of the galaxy lies. Column 9. Effective exposure time (in ks) of the target chip, after removing background flares. Column 10. Notes on individual obsids: a. subarray (512 rows), b. subarray (256 array), c. CCD readout streaks, d. no fid light.

1. Annulus binning (AB). Use circular annuli spanning an entire 360° or partial annuli with a set of specific sectors. The latter is particularly useful when the gas distribution is not spherically symmetric or at the edge of the detector to avoid unwanted sources. The inner and outer radii of each annulus are adaptively determined, based on a given S/N. We apply S/N = 20, 30, and 50.

2. WVT binning (WB). Use the weighted Voronoi tessellation (WVT) adaptive binning. This method was originally developed to analyze optical integral field spectroscopic data by Cappellari & Copin (2003) and was later applied to X-ray data by Diehl & Statler (2006).

3. Contour binning (CB). This method is similar to WB, but additionally takes into account the fact that the areas with
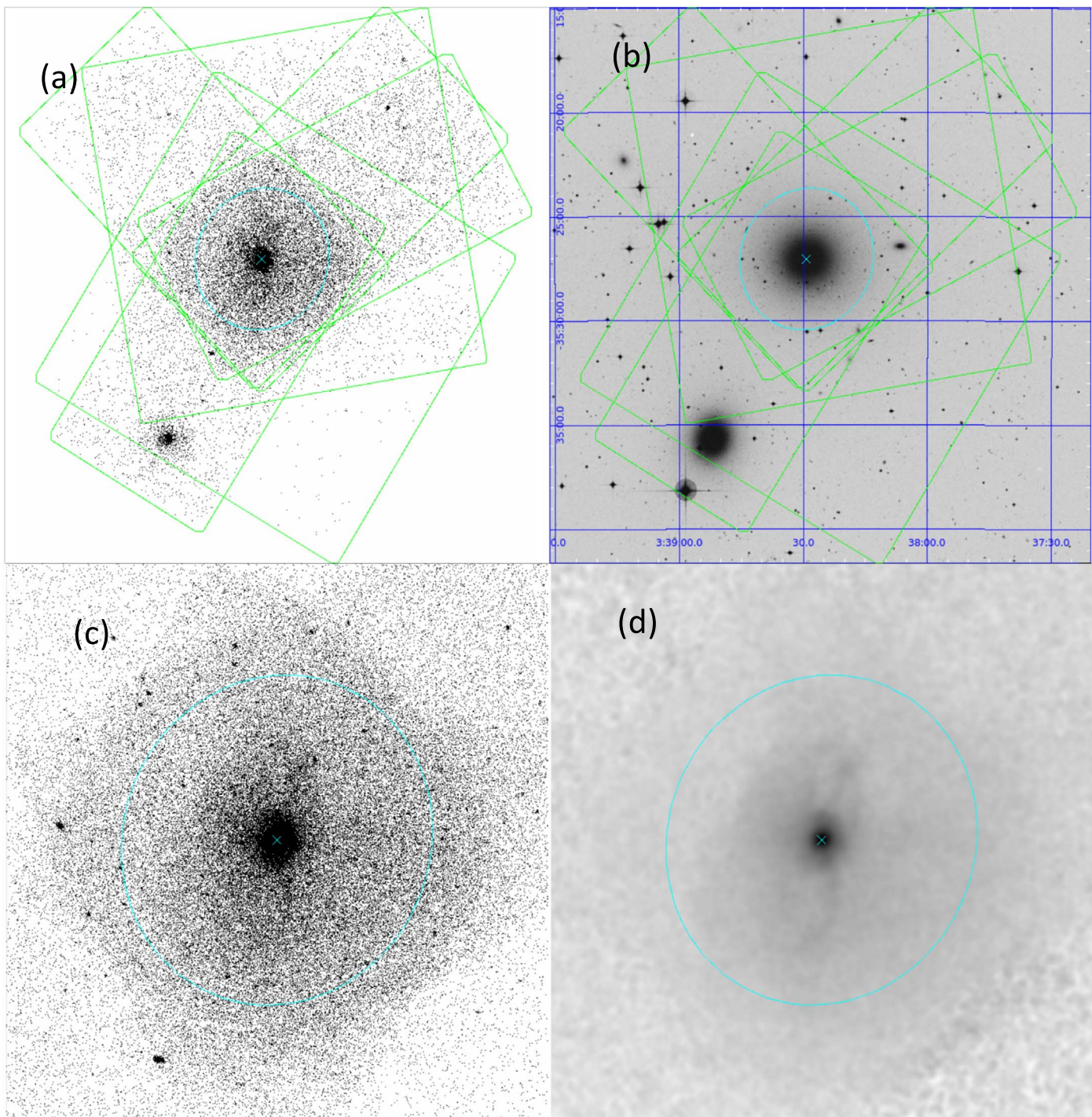
Figure 1. (a) *B*-band (0.3–8 keV) image of NGC 1399. Six observations are merged. The green rectangles are the detector frames of ACIS-I (I0-I3 4 chips with an approximate size of 16′ × 16′) and ACIS-S (S2-S3 2 chips with an approximate size of 8′ × 16′). The cyan ellipse is the optical D$_{25}$ ellipse. A companion galaxy, NGC 1404, is also seen in the lower left corner. (b) The optical DSS image in the same field of view. (c) A zoomed-in view of the *C*-band (0.5–5 keV) image of NGC 1399. A few hundred point sources are embedded in the extended diffuse emission. (d) The *G*-band (0.5–2 keV) image after the detected point sources are excluded, filled with photons in the surrounding regions. This image was also exposure-corrected and smoothed with a Gaussian kernel of 35 pixels (17″) to best illustrate the diffuse gas emission of NGC 1399. The bright central region and the northern and southern filaments are clearly visible inside the D$_{25}$ ellipse. In all figures, north is up and east is to the left.

similar surface brightness have similar spectral properties (Sanders 2006). As the regions within an isointensity contour are grouped together into a single bin, each spatial bin often has a partial annulus-like shape.

4. Hybrid binning (HB). This is described in detail in O'Sullivan et al. (2014). A fixed grid of a chosen spatial

resolution is laid out covering the region of interest. For each grid square, the algorithm adaptively determines the radius of a circular spectral extraction region, centered at that position, which is necessary to achieve the desired S/N or number of counts, up to some maximum size. Spectra are extracted and fitted, and the fit values are used
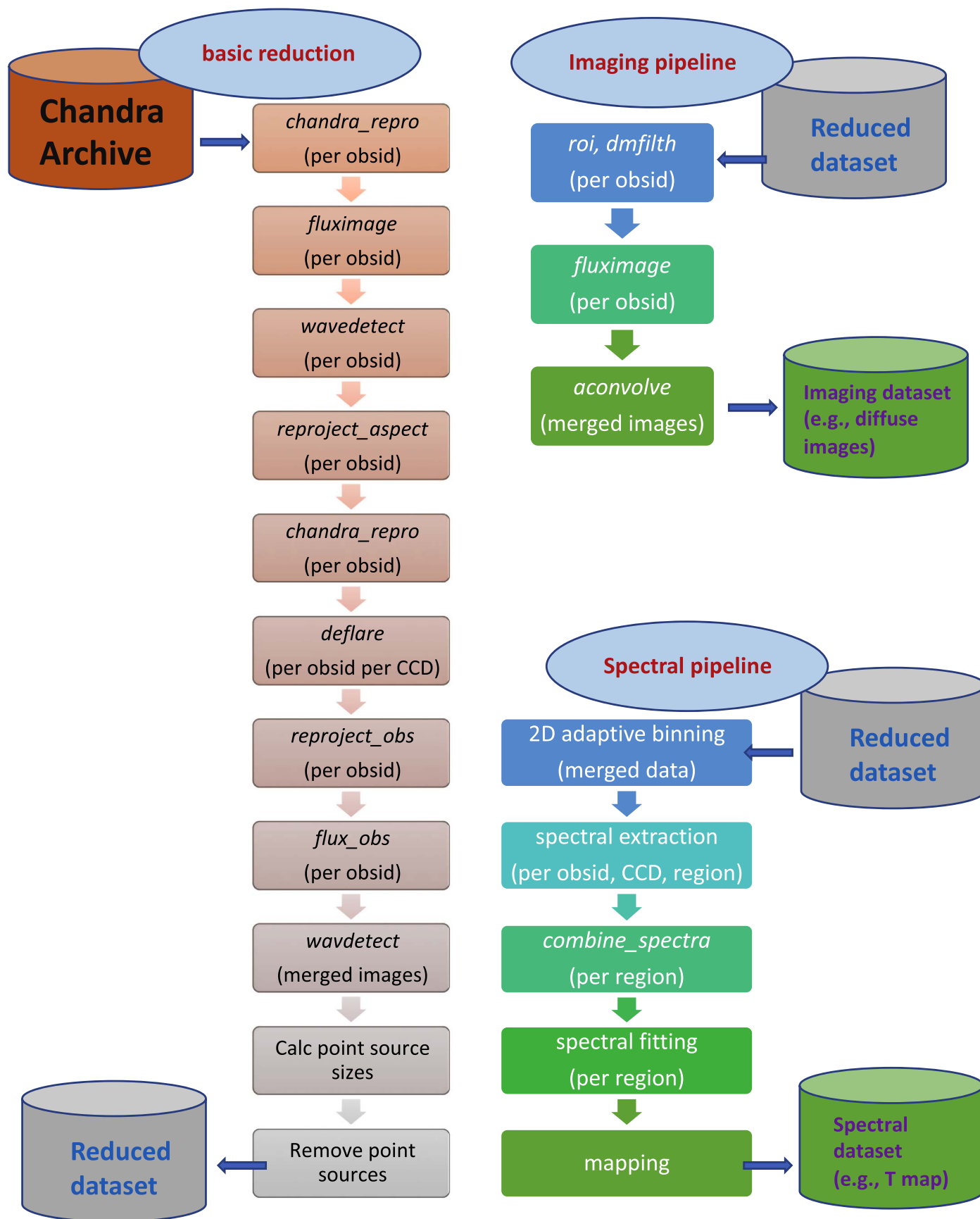
Figure 2. Overview of the data analysis workflow. The individual processing steps are shown in rectangles and associated data sets in cylinders. Steps in italics indicate the CIAO tools used in each step.

Table 3
Energy Band

Band Name	Short Name	Minimum Energy	Maximum Energy	Effective Energy[a]
broad	B	0.3	8.0	2.3
hard	H	2.0	7.0	3.8
center	C	0.5	5.0	2.0
gas	G	0.5	2.0	1.0

Notes. B—used to overview the entire observation. C and H—used in detecting point sources (Section 3.2). C—used in adaptive spatial binning (Section 3.3). G—used to show diffuse images (Section 3.2).
[a] Effective energy: effective area weighted mean energy within a given energy band.

Table 4
Point-source Size

Net Counts	EE Fraction (%)
<100	90
100–200	94
200–500	95
500–1000	96
1000–2000	97
>2000	98

to populate the map because the extraction regions may be larger than the grid squares they may overlap, and may therefore not be statistically independent. The resulting maps are therefore analogous to adaptively smoothed images, with high spatial resolution and low smoothing in regions of high surface brightness, and heavier smoothing of fainter emission.

The first method is the most straightforward, and has been widely used to measure the 1D radial profiles and global properties of ETGs. The next two methods provide the 2D distributions of gas properties in a statistically rigorous manner. The fourth method uses neighboring bins that are not independent; hence statistics are not straightforward. However, it provides complementary information at higher spatial resolution in regions of lower surface brightness, which may be lost in the first three methods. All binning methods are applied to the C band (0.5–5 keV). The bin size is controlled by S/N or net counts per bin. We typically use three sets of S/N values (20, 30, and 50) to optimally balance resolution and statistics. We note that in calculating the S/N, the background count was properly treated in AB and HB, where S/N = src_count/(src_counts + bg_counts)$^{1/2}$, but not in WB and CB, where S/N = (src_counts + bg_count)$^{1/2}$. While this makes a negligible effect near the center, the S/N (in WB and CB) is actually lower than specified when the background is high in the outskirts. We will implement the correct S/N calculation in a future release. We note that we apply a kT error cut to the resulting maps, which should remove any low S/N regions where the spectra were of poor quality (see Section 3.5).

In Figure 4 we show an example of the four G-band (0.5–2 keV) images of NGC 1399 (the same galaxy as in Figure 1) binned by the four adaptive binning methods. As

described above, each binning method has advantages and disadvantages. While AB provides only the 1D characterization, WB provides additional 2D azimuthal variations, CB further shows similar surface brightness regions, and finally, HB retains the highest resolution in low surface brightness regions. In analyzing a galaxy, it is recommended that all four binning results should be considered because they convey different and complementary information,

3.4. Spectral Extraction

After the spatial adaptive binning, the X-ray spectra are extracted from each spatial bin. The spectral extraction is performed on each individual observation. If the spatial bin lies on more than one chip, the spectra are extracted separately for each chip. To take into account time-dependent and position-dependent ACIS responses, the corresponding arf and rmf files are also extracted for each observation for each chip.

To properly subtract the background emission, we download the blank-sky data from the *Chandra* archive.[18] We match the sky background event file for each obsid for each chip to the real observation by reprojecting them to the same tangent plane as each observation (see Section 3.1) and excluding the same point-source regions as in each observation (see Section 3.2). We then rescale them to match the rate at higher energies (9–12 keV) where the photons are primarily from the background (Markevitch et al. 2003). To confirm the validity of the sky background and to check temporal and spatial variations of the soft X-ray background, we used off-axis source-free regions from the same observation in a few test cases and did not find any significant difference.

After source spectrum, background spectrum, arf, and rmf for each obsid for each chip are generated, we use the CIAO tool *combine_spectra* to combine them to make a single data set for each bin. In this way, the spectral fitting is more straightforward and quicker. We also performed a joint fit by simultaneously fitting individual spectra and found no significant difference.

3.5. Spectral Fitting

We primarily use the two-component emission model VAPEC[19] for hot gas (collisionally ionized diffuse gas) and a power law for undetected LMXBs. Taking advantage of the adaptive binning to separate different regions with different spectral properties, this two-component model is sufficient in most cases. We fix the power-law index to be 1.7, which is appropriate for the hard spectra of LMXBs (e.g., Boroson et al. 2011) and AGNs (see AGN-related issues in Section 4.3) and N_H to be the Galactic H I column density (Dickey & Lockman 1990). We also fix the metal abundance to be solar at GRSA (Grevesse & Sauval 1998). Although the abundance is known to vary from a few tenths to a few times solar inside the hot ISM, the hot gas temperatures do not significantly depend on the abundance (e.g., see Kim & Pellegrini 2012). The proper determination of the metal abundance requires high S/N data, and we will further investigate the 2D abundance distribution in a future paper.

---

[18] http://cxc.harvard.edu/ciao/threads/acisbackground/index.html#choosefile.lookup
[19] https://heasarc.gsfc.nasa.gov/xanadu/xspec/manual/XSmodelApec.html
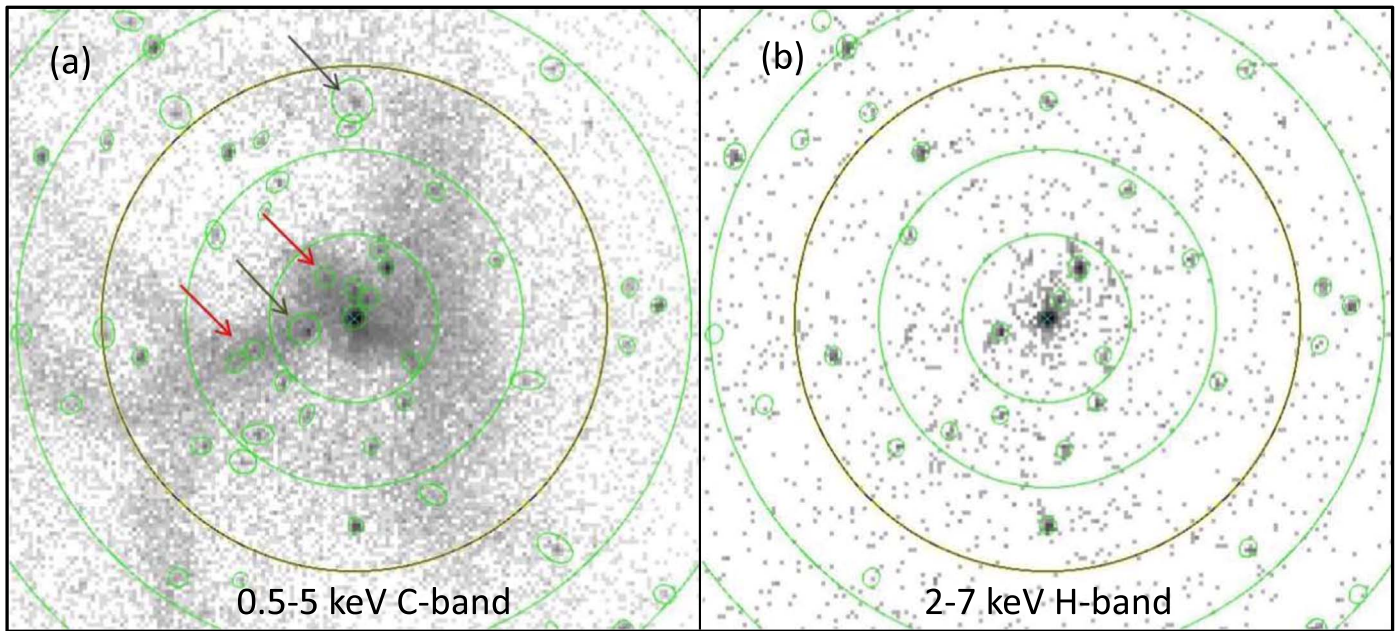
Figure 3. Point sources in the central region of NGC 4374 (M84) detected in two energy bands: (a) in the 0.5–5 keV *C* band and (b) in the 2–7 keV *H* band. The red arrow indicates sources detected only in the *C* band, and the black arrows indicates sources with uncertain positions and sizes. The small green ellipses are (a) the source sizes determined by wavdetect and (b) our new PSF-based source sizes. The large green circles are at $r = 10, 20, 30$, and $40''$. The yellow circle at $30''$ indicates the radius inside which the *H*-band sources are used.

We then produce spectral maps with various spectral parameters, e.g., the gas temperature, the normalization parameter of the VAPEC model divided by the area of each spatial bin (we call it normalized emission measure[20]), and the lower and upper limits of each parameter and corresponding reduced χ^2 values. We apply a mask to remove the bins where the spectral parameters are not well constrained with a significant error in spectral fitting. We select the mask such that only gas temperatures with an error smaller than 30% are shown. In this way, the resulting map shows only bins with reliable measurements. Additionally, we also produce the projected pseudo-pressure maps ($P_P = S_X^{1/2}\, T$) and projected pseudo-entropy maps ($K_P = S_X^{-1/3}\, T$) in arbitrary units, where Sx is the normalized emission measure. We note that although they are not the 3D pressure and entropy, they still provide useful information, particularly for discontinuities, e.g., cold front and shock front (see e.g., Werner et al. 2012; Kim et al. 2018). We also note that the APEC normalization (pressure and entropy as well) depend on the abundance variation. Unless the abundance is constant, the abundance gradient (likely negative) would make the normalization and the pseudo-pressure flatter and the pseudo-entropy steeper (e.g., see Kim & Pellegrini 2012).

In Figure 5 we show the temperature maps of NGC 1399 made by four adaptive binning methods as in Figure 4. The temperature is 0.8 keV in the central region and gradually increases with increasing radius to ~1.5 keV at the D25 ellipse. In contrast to AB, the other three binning methods clearly show the 2D thermal structure, the cooler gas extending along the filaments seen in the surface brightness maps (see more in Section 5.1).

3.6. Multi-Processing

Because the number of spatial bins is large, on the order of 10,000, for some deep observations of hot gas-rich galaxies, processing can be time consuming and becomes impractical for a single processor. To optimally process a large number of repeated tasks, particularly in the spectral extraction, generating arf/rmf and spectral fitting, we make use of the Smithsonian Institution High Performance Cluster (SI/HPC),[21] a Beowulf cluster consisting of nearly 4000 CPU cores, distributed over 108 compute nodes and over 24 TB of total RAM.

4. *Chandra* Galaxy Atlas

4.1. CGA Data Products

We provide the CGA data products in a dedicated CGA website.[22] The 1D radial profiles and the 2D images can be directly viewed in the browser, and the necessary data products can be downloaded for further analysis. For those who wish to take a quick look at the hot gas distribution and the thermal structure, the figures posted on the CGA website should be useful. Examples are shown in Figures 6–8.

In Figure 6 the radial profiles of the surface brightness ($L_{X,GAS}$/area) and the gas temperature of NGC 4649 are presented. We show the profiles measured in two spatial binning methods, AB and WB. While AB represents the hot gas structure well when the gas is symmetric, WB further shows the degree of asymmetry as in the outer region of NGC 4649. Also shown are the total $L_{X,GAS}$ and $\log(L)$-weighted mean T (see Section 5.2) within a given r. The vertical lines indicate $r = 5$ arcsec (red), $r = 1$ and $5 \times R_e$ (cyan), and $r = R_{MAX}$ (blue), which is the maximum radius where the hot

---

[20] The APEC normalization (for its definition, see the above footnote 19) depends on the bin size. The normalization divided by the bin area is proportional to the integral of $n_e\, n_H$ along the line of sight. The unit of the area is in pixels. An ACIS pixel size is 0.492 arcsec on each side.
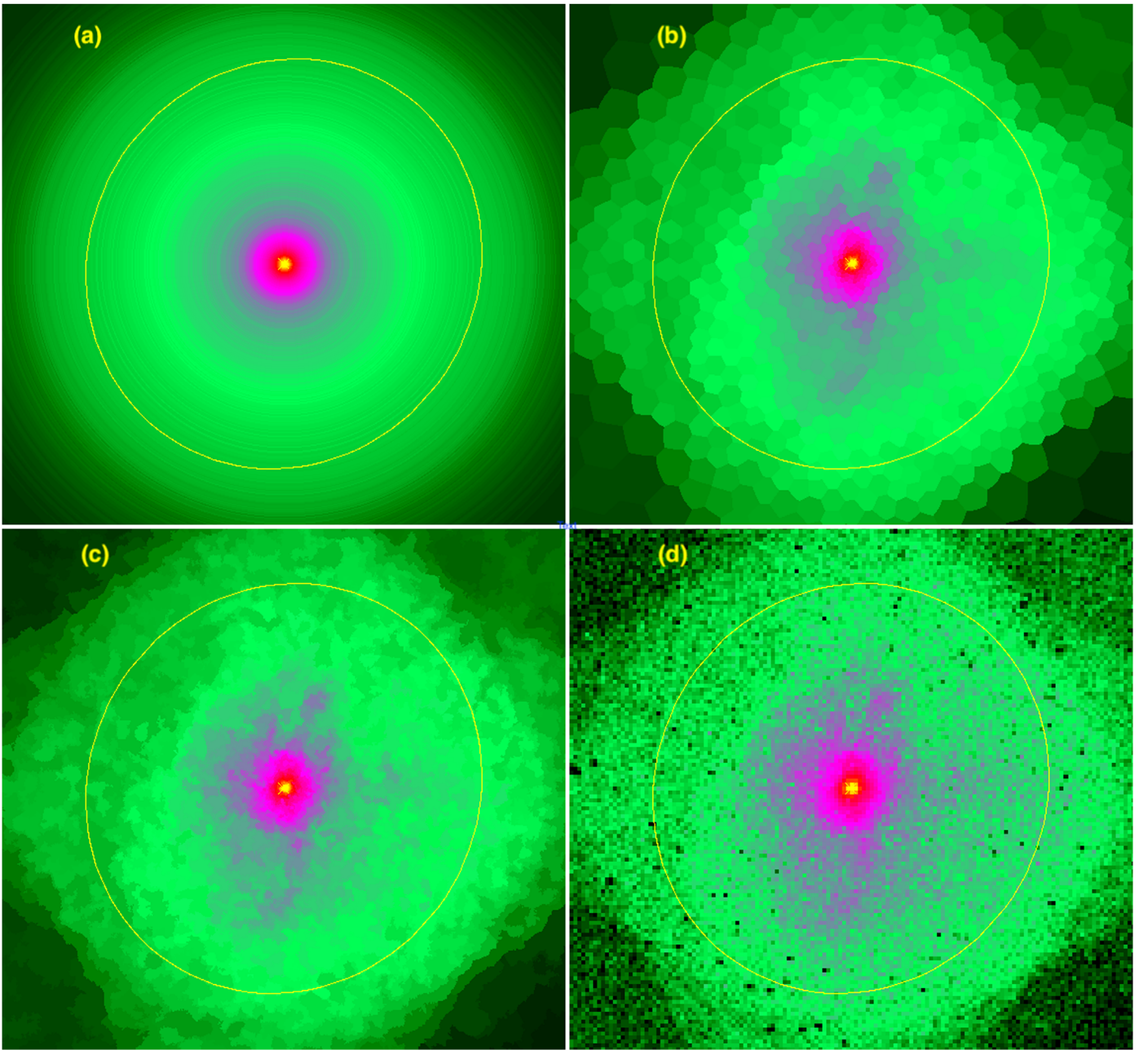
Figure 4. Adaptively binned *G*-band (0.5–2 keV) images of NGC 1399 (in Figure 1). (a) AB, (b) WB, (c) CB, and (d) HB. In all cases, we set the S/N = 20.

gas is reliably detected with an azimuthal coverage larger than 95% (see Section 5.2).

Figure 7 shows a part of the CGA image gallery with postage-stamp 2D images of diffuse gas of individual galaxies, and Figure 8 shows the 2D spectra maps of an example galaxy, NGC 4649 (third row, third column in the left panel), which is displayed by clicking the galaxy image on the left panel. The spectral maps include the binned images, *T* maps, normalized emission measure maps (=APEC normalization parameter/bin area), projected pressure maps, and projected entropy maps measured in four binning methods (AB, WB, CB, and HB).

We produce downloadable data products and make them available in two packages. The main package (package 1) consists of the high-level data products: point-source removed and filled, exposure-corrected images (jpg/png and FITS format) in multiple energy bands to best illustrate the diffuse hot gas distribution, derived T-maps (jpg/png and FITS format) in various adaptive binning methods to show the hot gas thermal structure. They can be used directly for an overview, to obtain the necessary hot gas quantities, and to compare them with data at other wavelengths with no additional X-ray data reduction.

For those who intend to perform their own analyses, e.g., to extract and fit X-ray spectra from user-specified regions, we provide all the necessary data in the supplementary package (package 2) which includes all the event files for each obsid and for each ccd. The entire sets of data products in the main and supplementary packages are described in detail in Appendix A.
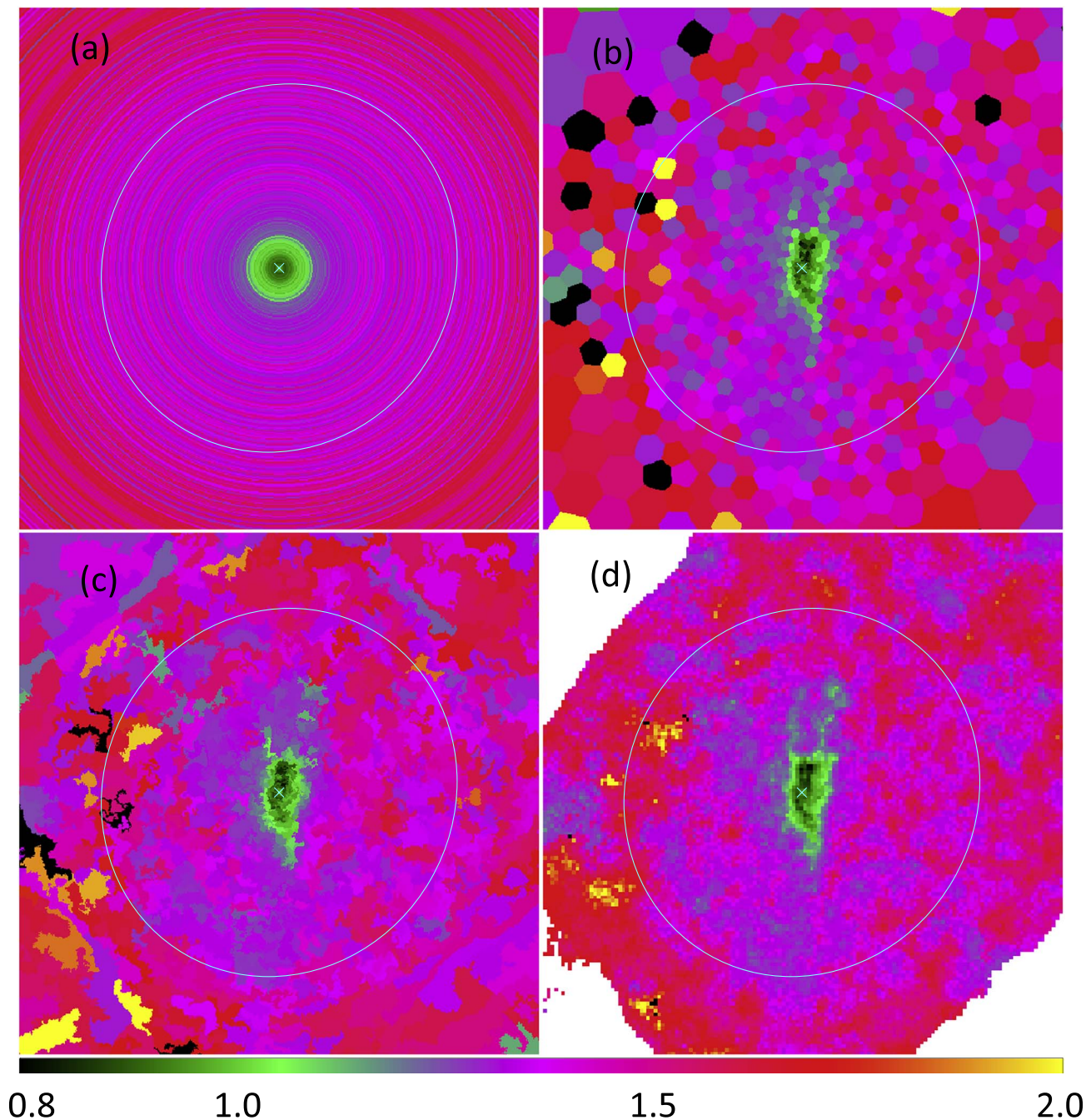
Figure 5. Temperature maps of NGC 1399, determined by four binning methods as in Figure 3. The color bar indicates the temperature, which ranges from 0.8 to 2 keV.

4.2. Example Usages of CGA Data Products

While the high-level products (e.g., diffuse images and temperature maps) are shown in a predetermined format at the CGA website, users can manipulate the CGA data products for their own use for various purposes. Here we provide a few possible applications.

4.2.1. How to View the X-Ray Image as Observed

The main package includes the merged images, exposure maps, and diffuse images (point-source excluded and exposure corrected) for multiple energy bands (in Table 3). These fits files can be viewed, e.g., using SAOImage ds9.[23] Similarly, the temperature maps (in fits) can be downloaded for review in ds9 and to compare with images at other wavelengths.

4.2.2. How to Review Spectral Fitting Results of Individual Spatial Bins

The spectral fitting results for all spatial bins are available in the data package. The "binno.fits" file in the main package can be used to identify the bin number of the region of interest

---

[23] http://ds9.si.edu/site/Home.html
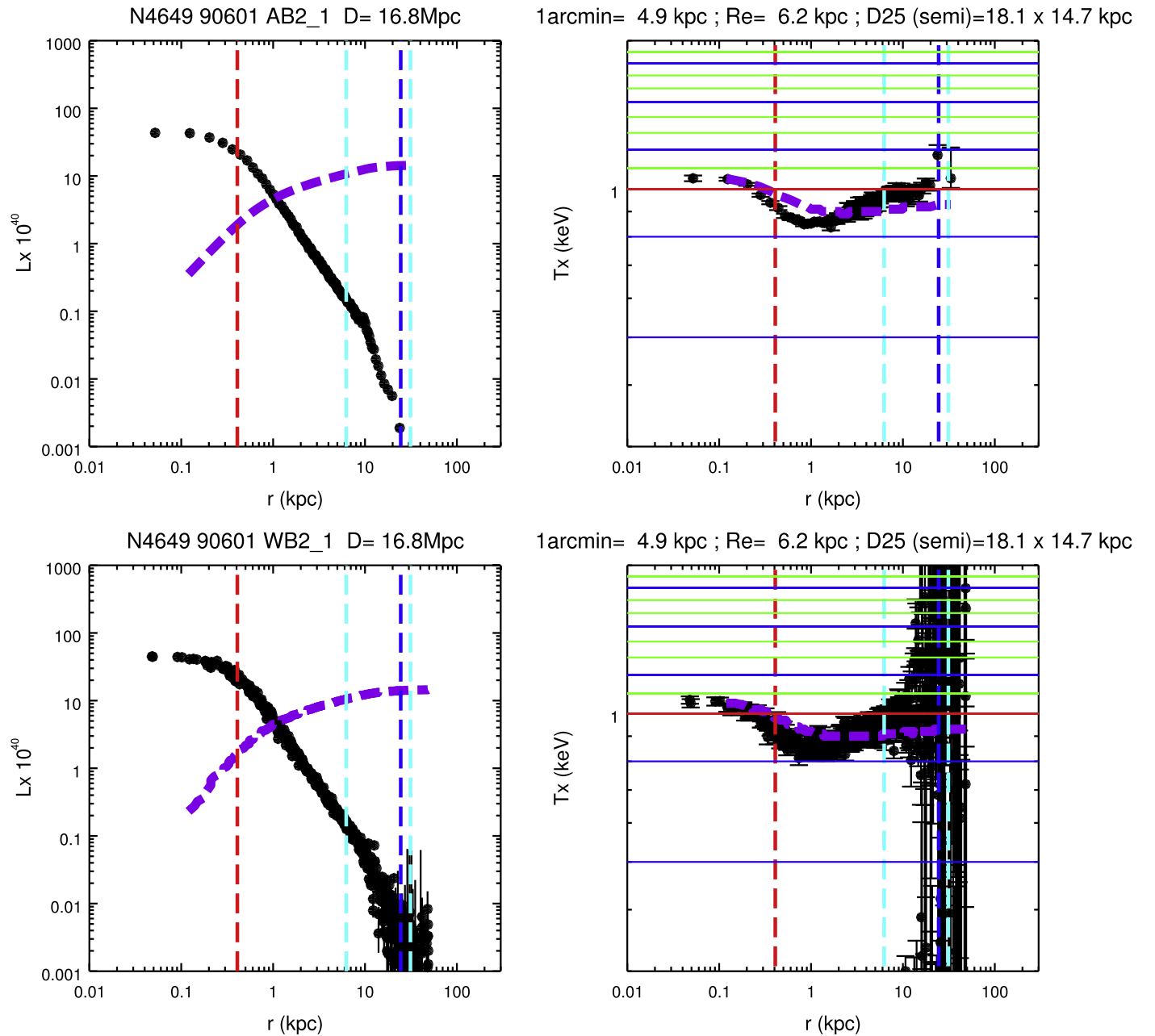
Figure 6. Radial profiles of (left) the surface brightness ($L_{X,GAS}$ from a given bin in 10^{40} erg s^{-1}/area of the bin in arcmin^2) and (right) the gas temperature in two spatial binning methods, (top) AB and (bottom) WB. The thick dashed purple lines indicate (left) $L_{X,GAS}$ ($<r$) in 10^{40} erg s^{-1} and (right) L_X-weighted mean T ($<r$). The vertical lines indicate $r = 5$ arcsec (red), $r = 1$ and $5 \times R_e$ (cyan) and $r = R_{MAX}$ (blue), which is the maximum radius where the hot gas is reliably detected with an azimuthal coverage larger than 95% (see Section 5.2).

(e.g., using ds9). An ascii table (sum.dat in the main package) contains a summary of fitting results including T, norm, reduced χ^2, distance from the galaxy center, and area for each bin.

4.2.3. How to Rerun Spectral Fitting in Individual Spatial Bins

Because of a large number of spatial bins, the source and background spectra, arf and rmf, are not included in the data package. Instead, we provide a full set of source and background event files (for all obsids and for all CCDs). A user can use these data files and perform their own spectral fitting with their own models and parameters as described in

Sections 3.4–3.5 (see also CIAO science threads for spectral fitting)[24]. Users can further use their own region files.

4.2.4. How to Make a Radial Profile in a Specified Pie Sector

Given that a full 2D spectral maps are provided, one can easily generate 1D projected radial profiles with any spectral parameter as a function of r (from sum.dat in the main package). They include temperature, norm/area, luminosity/area, projected entropy, and projected pressure. If the hot gas morphology is not azimuthally symmetric, one can select the

---

[24] http://cxc.harvard.edu/ciao/threads/ispec.html
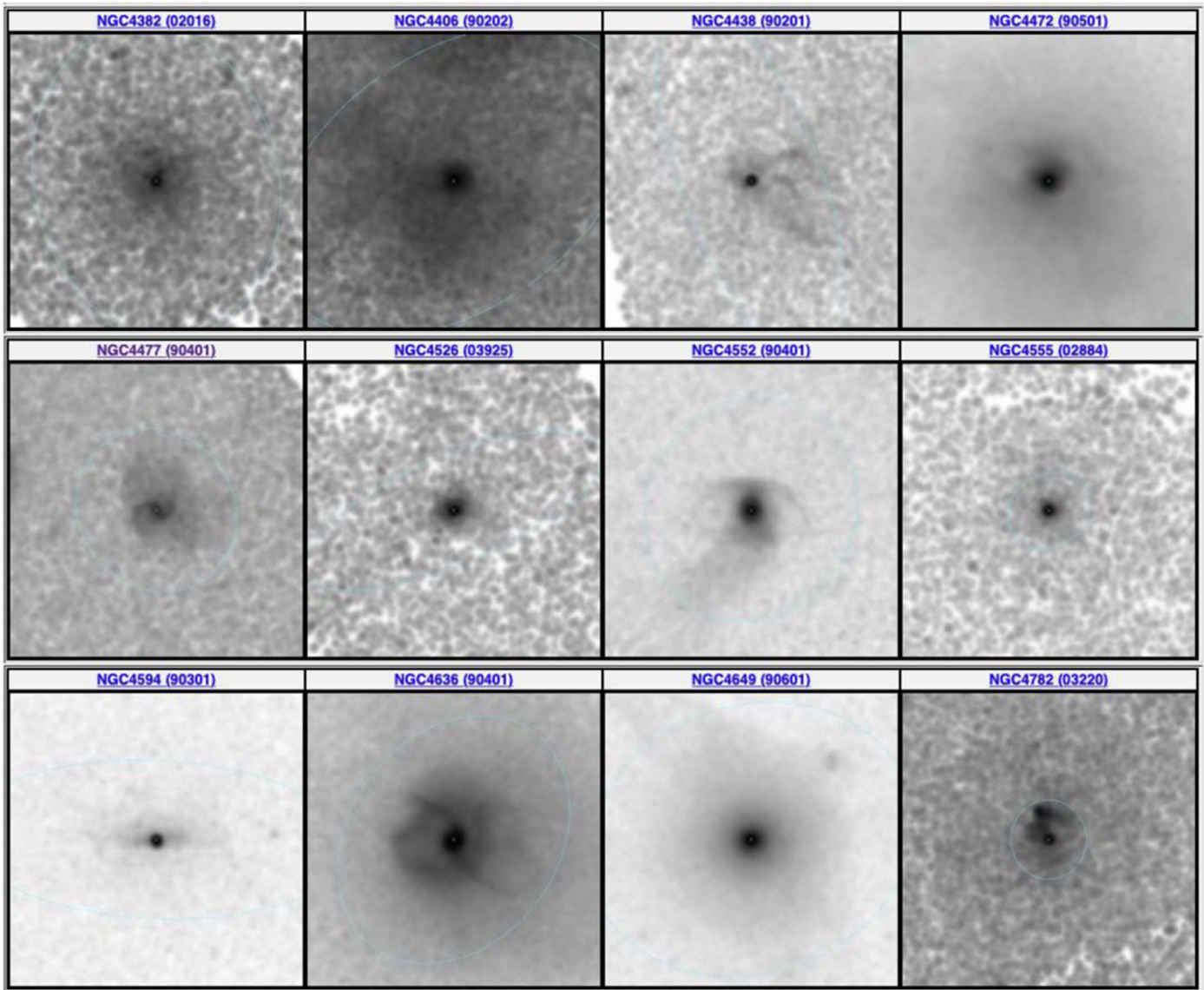
Figure 7. Image gallery of diffuse gas from individual galaxies available at the CGA website.

proper region in a given pie sector, for example, away from or across the discontinuity or cavity. WB (Section 3.3) is particularly useful for this purpose.

4.3. Data Caveats

1. CCD readout streak. When the central AGN is very bright, the CCD readout may cause streaks along the CCD column (see Column 10 in Table 2). In this case, we determine the streak region by *acis_streak_map* for each obsid and remove this region from the image and event files for adaptive binning (Section 3.3) and spectral analysis (Sections 3.4–3.5). Effectively, we treat the streak in the same way as the point sources that we removed in Section 3.2. However, unlike the point sources, we do not refill the excluded region for the diffuse hot gas image because the streaks are often in the middle of complex hot gas structures.

2. CCD gaps and boundaries. The gaps between chips and node boundaries are often less exposed and are most evident in raw images before the exposure correction, but sometimes they are still visible even after the exposure corrections. They are least visible in the spectral maps (e.g., in a T map) because the different exposures are appropriately treated bin by bin. One good example is NGC 1550, which was observed four times, and the significant exposure variation is clearly visible near the southern edge of the D_{25} ellipse. Although the raw data and binned image (counts/area) show a sharp discontinuity, the T map and EM (normalization/area) map are generally smooth with no clear artifact at that location. We note that the gap may appear more significant in CB than other binning methods because the CB spatial bin is determined in a region with similar counts/area. Users should be cautious about the gaps when considering any physical changes across the gap.

3. Strong nuclear sources. When an AGN at the center dominates the entire X-ray emission with a strong nuclear X-ray source and little amount of hot gas that is confined near the central region, the hot gas properties are difficult to measure. In this release, we adopt a power law with a spectral index of 1.7 for the nuclear source. If the AGN
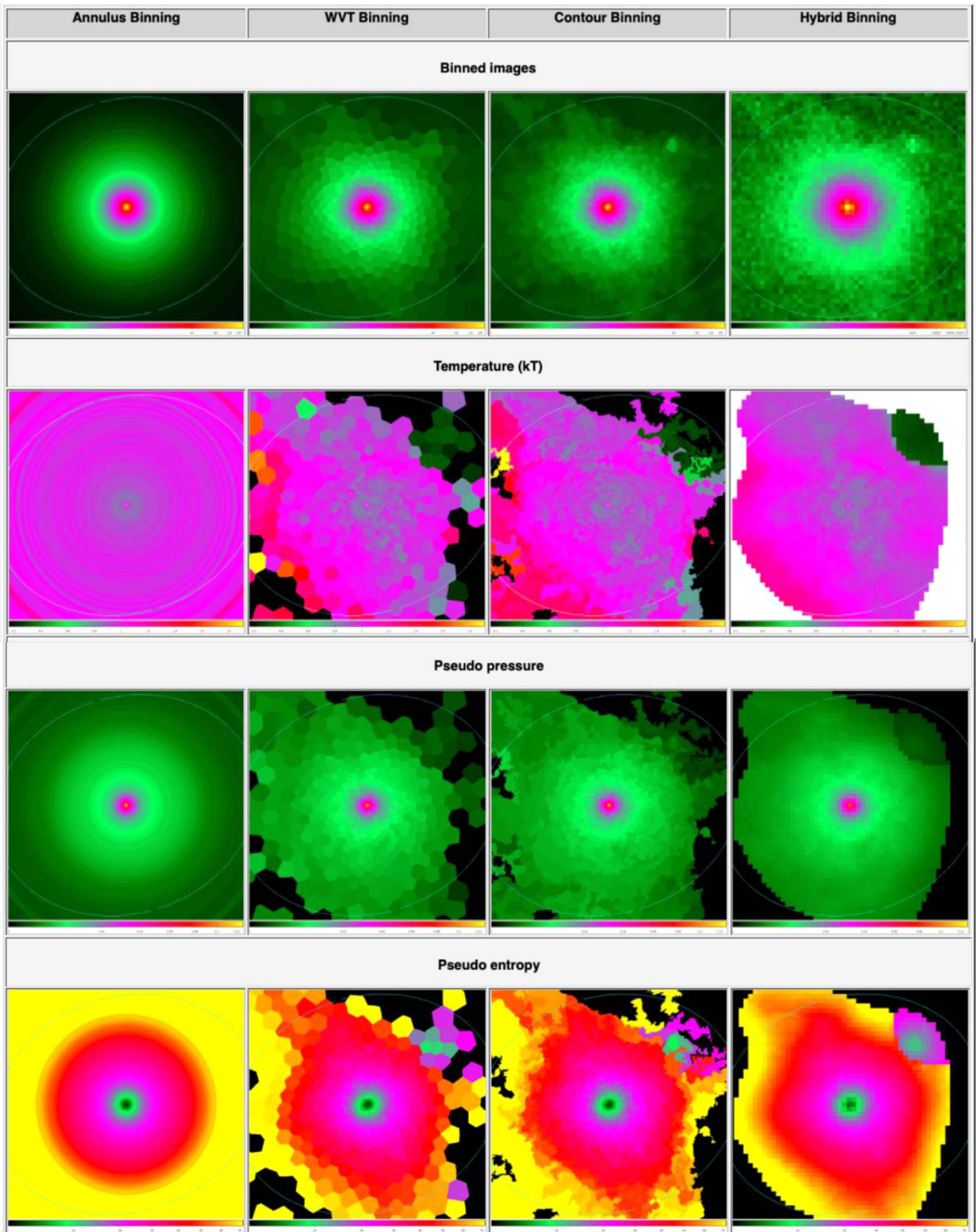
Figure 8. Example of a set of spectral maps (binned image, temperature map, pressure map, and entropy map, from top to bottom) of NGC 4649.
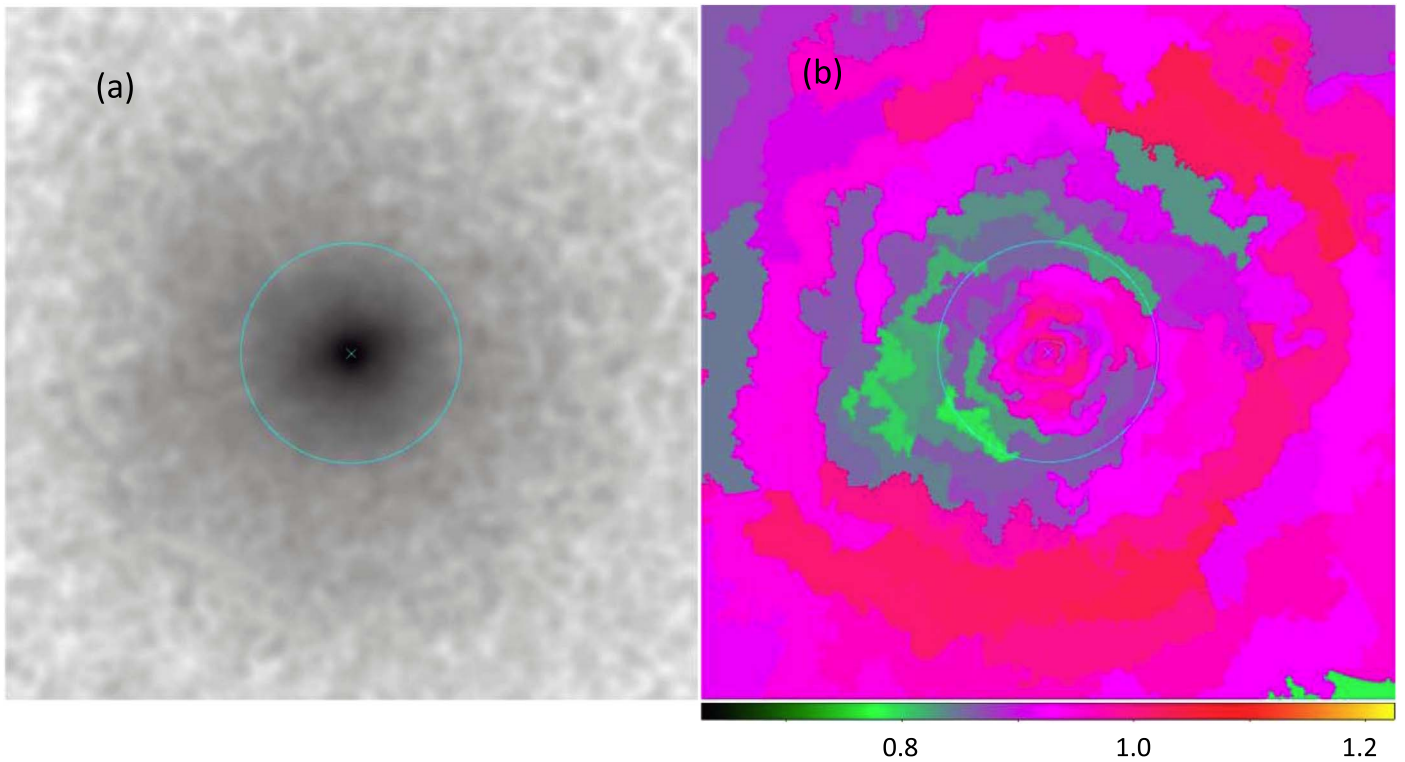
Figure 9. (a) Diffuse image (0, 5–2 keV) and (b) temperature map (CB) of the hot gas in NGC 3402. The cyan ellipse indicates the optical D$_{25}$ ellipse.

X-ray spectrum is significantly different, the measured hot gas properties are subject to systematic uncertainties. We will carefully investigate the circum-nuclear hot gas as one of our focused studies in the near future.

5. Discussions

The CGA data products provide a basis for the investigation of a number of important scientific questions. We describe some examples below, including results from previous studies and investigations we plan to publish in later papers.

5.1. Hot Gas Morphology

The high spatial resolution *Chandra* data show various spatial features in the hot ISM that were previously considered as smooth and relaxed. These features seen in the X-ray surface brightness maps include X-ray jets (e.g., NGC 315), cavities (e.g., NGC 5813), cold fronts (e.g., NGC 1404), filaments (e.g., NGC 1399), and tails (e.g., NGC 7619). Furthermore, new features can be identified in the spectral maps that are not readily visible in the surface brightness maps. An excellent example is NGC 3402 (as reported by O'Sullivan et al. 2007), where the X-ray surface brightness of the diffuse gas appears to be relaxed, but the temperature map clearly indicates a cooler shell structure at 20–40 kpc (see Figure 9 and additional notes in Appendix B).

Another good example is NGC 4649 (see Figure 8). The top row shows the asymmetric hot gas distribution with the extended tail toward the northeast and the southwest (upper left and lower right, see also Wood et al. 2017). The first (AB) *T* map shows a rather complex profile. *T* decreases with increasing radius in the inner region and then increases in the outer region (see also Humphrey et al. 2013 and Paggi et al. 2014). The negative gradient in the central region is likely related to the AGN, while the positive gradient in the outskirts is likely related to the hotter gas associated with the galaxy cluster in which NGC 4649 resides. The next three 2D *T*-maps further show more complex temperature structure; the cooler region is more extended toward the northeast and the southwest, indicating that the asymmetrical features are extended from the center to the outskirts. Although this galaxy has been extensively investigated, this 2D *T* structure was discovered for the first time in our program.

Another excellent example of new features discovered in our program is the disturbed fossil group galaxy NGC 1132. It is a well-known fossil group, i.e., an old system expected to have formed several gigayears ago, and to be completely relaxed by now. Instead, the hot gas morphology is disturbed and asymmetrical, with a cold front following a possible bow shock (Kim et al. 2018). We have found a few more interesting cases and will present them in separate papers.

5.2. Global Properties of Hot Gas

The global quantities of hot gaseous halos in ETGs have been extensively used in the literature to compare with data at other wavelengths and theoretical predictions to better understand the physical properties of the hot ISM and the evolution of the ETGs (e.g., Kim & Fabbiano 2013, 2015; Negri et al. 2014; Goulding et al. 2016; Choi et al. 2017; Ciotti et al. 2017; Forbes et al. 2017). In Table 5 we list the hot gas X-ray luminosity $L_{X,GAS}$ and temperature T_{GAS}, measured within three radii, one effective radius (Re), five Re, and R_{MAX}. The hot gas within one Re is closely related to the galaxy, as opposed to the large-scale surrounding medium (e.g., Goulding et al. 2016; see also Voit et al. 2018 for the usage of L_X(Re) to compare with model predictions.) The second radius (5 × Re) is where the total mass can be reliably measured with optical mass tracers, for example, GCs and PNe (see Deason et al. 2012;

Table 5
Global X-Ray Properties of the Hot ISM

Name (1)	Mid (2)	d (3)	Re_kpc (4)	Re5_kpc (5)	Rmax_kpc (6)	Lx1 (7)	eLx1 (8)	Lx5 (9)	eLx5 (10)	Lxm (11)	eLxm (12)	Tx1 (13)	eTx1 (14)	Tx5 (15)	eTx5 (16)	Txm (17)	eTxm (18)
I1262	90401	130.0	7.7	38.6	271.1	34.268	2.568	356.478	11.499	1194.051	25.122	1.48	0.06	1.56	0.02	1.68	0.02
I1459	02196	29.2	5.2	26.2	19.9	1.329	0.068	⋯	⋯	2.537	0.100	0.51	0.02	⋯	⋯	0.49	0.01
I1860	10537	93.8	8.4	42.0	118.2	48.288	2.101	197.020	6.315	360.236	10.236	1.07	0.02	1.28	0.01	1.37	0.01
I4296	03394	50.8	11.9	59.4	32.0	14.834	0.539	⋯	⋯	22.614	1.018	0.79	0.01	⋯	⋯	0.81	0.01
N0193	90201	47.0	4.4	22.1	61.5	0.437	0.054	10.611	0.237	16.006	0.341	0.67	0.05	0.84	0.01	0.86	0.01
N0315	90201	69.8	12.5	62.5	47.4	19.553	0.609	⋯	⋯	24.168	0.753	0.64	0.01	⋯	⋯	0.67	0.01
N0383	02147	63.4	6.3	31.5	83.0	5.479	0.325	18.359	1.846	⋯	⋯	0.76	0.03	1.35	0.06	⋯	⋯
N0499	90401	54.5	4.4	21.8	71.3	13.034	0.420	68.994	0.886	125.578	1.480	0.82	0.01	0.74	0.01	0.80	0.01
N0507	90201	63.8	12.9	64.4	133.0	39.935	1.268	254.337	4.528	391.513	6.278	1.14	0.01	1.27	0.01	1.30	0.01
N0533	02880	76.9	16.2	81.1	96.9	81.607	1.702	154.586	3.651	167.047	4.073	0.96	0.01	1.12	0.01	1.13	0.01
N0720	90401	27.7	4.8	24.1	45.6	2.557	0.057	7.264	0.107	8.547	0.138	0.61	0.01	0.56	0.01	0.54	0.01
N0741	02223	70.9	13.2	65.9	89.4	21.661	1.010	45.690	3.434	51.319	3.682	0.87	0.02	1.19	0.04	1.16	0.03
N1052	05910	19.4	3.1	15.7	24.5	0.236	0.024	0.418	0.042	⋯	⋯	0.49	0.03	0.41	0.02	⋯	⋯
N1132	90201	95.0	15.5	77.5	129.0	39.365	1.944	170.013	4.270	239.697	5.408	1.03	0.02	1.09	0.01	1.09	0.01
N1316	02022	21.5	7.6	38.1	14.6	4.039	0.107	⋯	⋯	5.137	0.131	0.64	0.01	⋯	⋯	0.62	0.01
N1332	90201	22.9	3.0	15.3	28.9	1.592	0.052	2.408	0.071	2.754	0.084	0.65	0.02	0.62	0.01	0.63	0.01
N1380	09526	17.6	3.2	16.1	22.2	0.463	0.027	0.847	0.062	1.003	0.078	0.33	0.01	0.48	0.02	0.55	0.02
N1387	04168	20.3	3.5	17.5	42.4	2.858	0.361	5.750	0.425	14.045	0.589	0.45	0.05	0.54	0.03	0.94	0.02
N1395	00799	24.1	5.4	27.2	39.7	1.772	0.144	5.052	0.291	7.053	0.377	0.82	0.04	0.87	0.03	0.89	0.02
N1399	90602	19.9	4.7	23.5	47.4	12.327	0.094	40.498	0.213	67.533	0.523	1.03	0.00	1.29	0.00	1.38	0.00
N1400	90202	26.4	2.9	14.7	34.6	0.361	0.051	0.898	0.079	⋯	⋯	0.49	0.06	0.55	0.04	⋯	⋯
N1404	91101	21.0	2.7	13.7	60.0	7.820	0.046	14.845	0.069	⋯	⋯	0.65	0.00	0.63	0.00	⋯	⋯
N1407	00791	28.8	8.9	44.3	36.4	8.605	0.194	⋯	⋯	14.060	0.414	0.86	0.01	⋯	⋯	1.01	0.01
N1550	90401	51.1	6.3	31.7	104.0	62.400	0.977	248.324	2.885	506.931	5.534	1.11	0.01	1.29	0.00	1.34	0.01
N1553	00783	18.5	5.1	25.7	24.3	0.448	0.040	⋯	⋯	2.222	0.095	0.42	0.04	⋯	⋯	0.35	0.01
N1600	90201	57.4	13.5	67.5	72.3	12.356	0.774	32.174	1.871	33.050	1.953	1.13	0.03	1.43	0.04	1.43	0.04
N1700	02069	44.3	3.9	19.3	57.9	4.994	0.227	9.709	0.386	9.709	0.386	0.50	0.02	0.43	0.01	0.43	0.01
N2300	90201	30.4	4.8	24.2	39.8	4.173	0.154	8.251	0.301	10.474	0.377	0.63	0.02	0.75	0.02	0.81	0.02
N2563	07925	67.8	6.4	31.9	124.9	10.125	0.708	20.832	1.962	70.908	3.934	0.95	0.03	1.24	0.05	1.48	0.04
N3115	91101	9.7	1.6	8.1	14.6	0.028	0.001	0.049	0.003	0.064	0.007	0.46	0.02	0.39	0.01	0.34	0.01
N3379	90501	10.6	2.4	12.1	14.3	0.023	0.002	0.059	0.005	⋯	⋯	0.44	0.02	0.34	0.01	⋯	⋯
N3402	03243	64.9	8.8	44.1	78.7	106.600	2.099	270.035	3.075	342.002	3.525	0.95	0.01	0.92	0.00	0.92	0.00
N3607	02073	22.8	5.0	25.1	35.4	0.310	0.049	2.559	0.159	⋯	⋯	0.63	0.10	0.49	0.03	⋯	⋯
N3608	02073	22.9	3.3	16.5	38.9	0.000	0.000	0.837	0.088	⋯	⋯	1.00	0.00	0.47	0.04	⋯	⋯
N3842	04189	97.0	17.8	88.9	80.0	7.977	1.099	⋯	⋯	⋯	⋯	1.04	0.04	⋯	⋯	⋯	⋯
N3923	90201	22.9	5.8	29.2	35.5	3.646	0.069	5.313	0.115	5.422	0.136	0.51	0.01	0.49	0.01	0.49	0.01
N4104	06939	120.0	20.0	100.2	157.1	79.862	5.307	175.693	12.780	236.625	15.603	1.29	0.04	1.49	0.05	1.52	0.05
N4125	02071	23.9	5.9	29.5	30.1	1.834	0.051	4.211	0.090	4.211	0.090	0.46	0.01	0.40	0.01	0.40	0.01
N4261	90201	31.6	6.9	34.3	39.9	6.624	0.157	11.791	0.331	12.507	0.358	0.70	0.01	0.96	0.01	0.97	0.01
N4278	90901	16.1	2.6	13.0	24.9	0.307	0.008	0.502	0.012	0.706	0.018	0.41	0.01	0.42	0.01	0.41	0.01
N4291	11778	26.2	2.0	10.2	33.0	0.307	0.038	4.323	0.168	6.832	0.252	0.57	0.09	0.48	0.02	0.56	0.01
N4325	03232	110.0	10.5	52.3	138.7	149.721	3.476	562.512	7.153	743.875	8.733	0.82	0.01	0.93	0.00	0.95	0.00
N4342	90201	16.5	0.5	2.3	21.6	0.003	0.003	0.185	0.008	1.343	0.029	0.86	0.38	0.61	0.02	0.66	0.01
N4374	90301	18.4	5.5	27.3	24.9	4.752	0.050	⋯	⋯	8.153	0.157	0.68	0.00	⋯	⋯	0.92	0.01
N4382	02016	18.4	7.4	37.0	24.1	0.851	0.037	⋯	⋯	1.999	0.070	0.41	0.01	⋯	⋯	0.37	0.01
N4406	90202	17.1	10.3	51.7	30.8	11.955	0.168	⋯	⋯	46.383	0.487	0.86	0.01	⋯	⋯	0.93	0.00
N4438	90201	18.0	5.0	24.8	18.3	0.986	0.053	⋯	⋯	2.807	0.242	0.61	0.02	⋯	⋯	0.83	0.03

Table 5
(Continued)

Name (1)	Mid (2)	d (3)	Re_kpc (4)	Re5_kpc (5)	Rmax_kpc (6)	Lx1 (7)	eLx1 (8)	Lx5 (9)	eLx5 (10)	Lxm (11)	eLxm (12)	Tx1 (13)	eTx1 (14)	Tx5 (15)	eTx5 (16)	Txm (17)	eTxm (18)
N4472	90501	16.3	8.2	41.2	38.7	14.562	0.054	⋯	⋯	34.672	0.221	0.99	0.00	⋯	⋯	1.14	0.00
N4477	90401	16.5	3.5	17.6	21.6	0.643	0.025	1.331	0.058	⋯	⋯	0.36	0.01	0.64	0.02	⋯	⋯
N4526	03925	16.9	3.3	16.7	21.3	0.267	0.021	0.446	0.038	⋯	⋯	0.38	0.02	0.42	0.02	⋯	⋯
N4552	90401	15.3	3.0	15.3	22.3	1.927	0.022	2.523	0.032	2.774	0.041	0.60	0.01	0.60	0.01	0.65	0.01
N4555	02884	91.5	13.2	66.1	115.3	11.911	0.822	39.345	2.110	51.000	2.488	0.85	0.03	1.03	0.02	1.00	0.02
N4594	90301	9.8	3.4	16.9	26.1	0.201	0.006	0.636	0.025	0.757	0.047	0.55	0.01	0.49	0.01	0.46	0.01
N4636	90401	14.7	6.7	33.3	34.8	14.122	0.055	28.106	0.090	28.381	0.091	0.69	0.00	0.79	0.00	0.79	0.00
N4649	90601	16.8	6.2	31.2	24.5	10.397	0.049	⋯	⋯	13.807	0.065	0.90	0.00	⋯	⋯	0.91	0.00
N4782	03220	60.0	4.4	21.8	75.6	1.470	0.168	8.614	0.795	24.721	2.138	0.57	0.05	0.97	0.04	1.15	0.04
N5044	90201	31.2	3.9	19.3	40.8	24.859	0.221	186.834	0.683	289.017	1.007	0.84	0.00	0.94	0.00	1.03	0.00
N5129	90201	103.0	14.3	71.6	144.8	29.011	1.220	88.676	2.581	147.756	3.629	0.81	0.02	0.90	0.01	0.78	0.01
N5171	03216	100.0	12.4	62.0	111.5	2.735	0.550	25.561	2.226	59.950	3.138	0.96	0.07	0.98	0.04	0.86	0.02
N5813	90901	32.2	8.3	41.6	43.7	37.910	0.102	108.779	0.170	110.017	0.173	0.65	0.00	0.71	0.00	0.71	0.00
N5846	90201	24.9	7.2	35.8	50.7	15.893	0.140	40.604	0.291	44.409	0.339	0.70	0.00	0.82	0.00	0.82	0.00
N5866	02879	15.3	2.8	14.2	19.4	0.125	0.014	0.262	0.023	⋯	⋯	0.36	0.03	0.35	0.02	⋯	⋯
N6107	08180	127.9	16.3	81.5	155.0	22.905	3.944	68.813	12.564	136.801	17.111	1.22	0.06	1.39	0.09	1.86	0.17
N6338	04194	123.0	17.1	85.3	286.3	333.765	15.807	650.347	35.560	1076.741	46.423	1.49	0.03	1.74	0.04	1.79	0.04
N6482	03218	58.4	6.3	31.7	76.5	42.411	1.435	80.526	1.818	104.898	2.333	0.83	0.01	0.72	0.01	0.66	0.01
N6861	90201	28.1	3.1	15.5	62.6	2.098	0.095	5.331	0.235	19.839	0.424	0.87	0.02	1.10	0.02	1.08	0.01
N6868	90201	26.8	3.9	19.6	62.3	1.161	0.057	7.196	0.140	20.430	0.366	0.72	0.03	0.70	0.01	0.69	0.01
N7618	90301	74.0	7.8	38.8	122.0	28.334	0.862	104.457	1.507	207.757	3.241	0.94	0.01	0.87	0.01	0.89	0.01
N7619	90201	53.0	8.8	44.1	105.3	16.562	0.466	40.008	0.881	69.881	1.928	0.83	0.01	0.92	0.01	0.99	0.01
N7626	02074	56.0	12.0	60.1	103.2	6.595	1.241	14.096	1.577	29.785	2.427	0.56	0.08	0.79	0.05	0.95	0.04

Note. Column 1. Galaxy name (NGC or IC name). Column 2. Merge id (or mid in short). Column 3. Distance in Mpc (same as in Table 2). Column 4. Re (effective radius) in kpc. Column 5. 5 × Re in kpc. Column 6. Rmax in kpc (the maximum radius to which the hot gas can be measured). Columns 7, 9, and 11. $L_{X,GAS}$ in 10^{40} erg s^{-1} within the three radii given in Columns 4–6. Columns 8, 10, and 12. Error in $L_{X,GAS}$ within the three radii given in Columns 4–6. Columns 13, 15, and 17. T_{GAS} in keV within the three radii given in Columns 4–6. Columns 14, 16, and 18. Error in T_{GAS} within the three radii given in Columns 4–6.

Alabi et al. 2016), and is often used in scaling relation to correlate with the total gas luminosity and temperature (Kim & Fabbiano 2013; Forbes et al. 2017). We provide $L_{\mathrm{X,GAS}}$ within five Re so that the total mass and the global X-ray properties from the same region can be compared. Finally, R_{MAX} is the maximum radius where the hot gas emission is reliably detected with an azimuthal coverage larger than 95% (calculated by the exposure map). In Table 5 we present the results from WB (WVT binning—see Section 3.3), which can reflect the 2D spatial variation more accurately than AB (annulus binning). However, the results from AB are mostly consistent.

We note that if the hot gas is extended beyond R_{MAX}, particularly for hot gas-rich ETGs, the luminosity within R_{MAX} is lower than the total gas luminosity (see below). We also note that L_{X} within a given radius is a projected quantity (i.e., 2D rather than 3D), such that $L_{\mathrm{X,GAS}}(<R)$ is the gas luminosity from a cylindrical volume, rather than a spherical volume. As we are working on deprojecting the hot gas properties, we will present the 3D $L_{\mathrm{X,GAS}}$ within a given 3D radius in the near future.

In some gas-poor galaxies where the X-ray emission is dominated by the central region and the hot gas is not extended, we stop at five Re and do not list the quantities at R_{MAX}. In some nearby large galaxies where 5 Re > R_{MAX}, we do not list the quantities at five Re.

Because we excluded the regions of the detected point sources (see Section 3), we correct $L_{\mathrm{X,GAS}}$ in each spatial bin by the ratio of areas with and without the point sources before summing them within a given radius. This correction is 20% for NGC 3115, where a large number of point sources are detected in the ultra-deep (1 Ms) *Chandra* observations, and the amount of hot ISM is small. In all the other cases, the correction is less than 10%. We have also excluded the contribution from nearby galaxies if they are within a given radius. The X-ray luminosity of the nearby galaxy is determined mostly by CB (contour binning—see Section 3.3), which makes a separate region around the nearby galaxy.

The gas temperature is also measured within the same three radii—one Re, five Re, and R_{MAX}. Because the region of interest consists of many spatial bins, we take an L_{X}-weighted average temperature, but in a logarithmic scale (i.e., geometric average instead of arithmetic average). For line-dominated spectra (for $T \leqslant 2$ keV), the temperature is mainly determined by the energy of the peak intensity, and this energy is linearly proportional to the plasma temperature in a log scale (see Figure 2 in Vikhlinin 2006). In this case, the geometric average (rather than the arithmetic average) is close (within a few precent) to what one would measure by a single spectral fit with a single spectrum extracted from the region of interest (e.g., $r < 1$ Re, or $r < 5$Re), often called T_{SPEC} (see Figure 3 in Vikhlinin 2006). The temperatures in Table 5 are calculated by L_{X}-weighted averaging log(T), where T is the gas temperature of each bin. We compare the geometric and arithmetic average values and find that the difference is usually less than 6%.

For completeness for hot gas-rich galaxies, in Table 6 we also list the total gas luminosity and temperature, compiled from the literature. We plan to include *XMM-Newton* data to supplement our *Chandra* results so that we can obtain complete gas properties by adding the outskirts of the extended hot halos. We will present the *XMM* results in a separate paper.

5.3. Radial Profiles of Hot Gas Temperature

The temperature profiles in groups and clusters are often similar to each other (e.g., Vikhlinin et al. 2005; Sun et al. 2009). In a typical relaxed group or cluster, the temperature increases inward from the virial radius (R_{VIR}) and peaks to T_{MAX} at $r \sim 0.1\ R_{\mathrm{VIR}}$ (or $\sim$100 kpc). Moving farther inward, the temperature decreases inside the cooling radius, depending on the cooling time (or the gas density). In ETGs, a similar trend is seen as the temperature often peaks in the inner part of the halo, although at a smaller radius ($r \sim$ a few $\times$10 kpc). In this regard, the global temperature profiles of ETGs qualitatively follow those of groups and clusters. We note that the temperature peak may not be visible if the outskirts of the hot ISM are too faint, fall out of the detector, or are embedded inside hotter ambient ICM/IGM.

In contrast to the overall temperature profile, the inner temperature behavior appears to be more complex (see also O'Sullivan et al. 2017; Lakhchaura et al. 2018). Inside roughly $r <$ a few kiloparsec (or Re), the temperature gradient can be negative (a hot core) in some galaxies and positive (a cool core) in other galaxies. This behavior at the central region is likely related to stellar and AGN feedback in addition to gravity, which is dominant on a large scale, although the exact heating/cooling mechanisms are yet to be understood. Possibilities include gravitational heating from the central SMBH, a recent AGN outburst, or interaction with confined nuclear jets (see Pellegrini et al. 2012; Paggi et al. 2014). The temperature and density profiles and their universality or their deviation from the universal profiles will be addressed in L. Traynor et al. (2019, in preparation).

5.4. X-Ray Based Mass Profile

X-ray observations of the hot ISM can be used to measure the total mass within a given radius by balancing the gravitational force and the pressure gradient in the hot gas under the assumption of hydrostatic equilibrium (HE). While this method has been extensively used, the assumption of HE is seriously in question because of various spatial features that are often found in ETGs. Recent studies suggest that nonthermal pressure is not negligible, typically consisting of 10%–30% of total pressure, but can be as high as >40% (de Plaa et al. 2012).

Using the CGA data products, Paggi et al. (2017) confirmed the presence of a nonthermal pressure component accounting for $\sim$30% of the gas pressure in the central region of NGC 4649, likely linked to nuclear activity. In NGC 5846, where the X-ray gas morphology shows significant azimuthal asymmetries, especially in the NE direction, Paggi et al. (2017) found substantial departures from HE in this direction, consistent with bulk gas compression and decompression (due to sloshing); this effect disappears in the NW direction, where the emission is smooth and extended.

We will apply this method to the entire sample by removing the pie sectors where the hot gas shows azimuthal asymmetries, discontinuities, etc., to derive the mass profiles to the extent that the HE is valid (D.-W. Kim et al. 2019, in preparation).

5.5. Low-mass X-Ray Binaries

Although not our primary goal, the X-ray properties of the LMXBs in each galaxy are readily available as byproducts, specifically, their photometric and spectral information (hardness ratios and colors). *Chandra*-detected LMXBs in ETGs

Table 6
Total Luminosity and Temperature of the Hot ISM

Name	d	$L_{\text{X,GAS}}$	Lxgas_lo	Lxgas_up	T_{GAS}	Tgas_lo	Tgas_up	References	Note
I1262	130.20	1639.585	245.937	3033.234	1.30	1.29	1.31	3	
I1459	29.24	4.311	1.103	7.520	0.48	0.46	0.50	3	
I1860	93.76	499.164	498.177	500.150	1.37	1.36	1.38	8	
I4296	50.82	10.669	6.789	14.549	0.88	0.86	0.90	3	
N0193	47.00	14.939	10.158	19.719	0.77	0.76	0.78	3	
N0315	69.80	8.858	5.654	12.063	0.64	0.63	0.65	3	
N0383	63.39	18.353	16.507	20.198	1.35	1.29	1.41	7	
N0499	54.45	172.161	86.284	343.506	0.70	0.67	0.72	6	
N0507	63.80	790.331	78.005	80.060	1.32	1.31	1.33	5	
N0533	76.90	94.275	59.904	128.647	0.98	0.97	0.99	3	
N0720	27.67	5.060	4.998	5.122	0.54	0.53	0.55	2	
N0741	70.90	25.774	15.303	36.245	0.96	0.94	0.98	3	
N1052	19.41	0.437	0.409	0.465	0.34	0.32	0.36	2	
N1132	95.00	716.528	682.408	750.648	1.08	1.07	1.09	4	
N1316	21.48	5.350	5.210	5.490	0.60	0.59	0.61	2	
N1332	22.91	2.401	1.514	3.805	0.41	0.36	0.47	6	
N1380	17.62	1.054	0.105	2.647	0.30	0.25	0.38	6	
N1387	20.32	4.269	3.873	4.665	0.41	0.38	0.44	7	[a]
N1395	24.10	2.437	1.537	3.863	0.65	0.60	0.69	6	
N1399	19.95	33.942	17.011	67.724	1.21	1.18	1.24	6	
N1400	26.42	0.899	0.820	0.978	0.55	0.51	0.59	7	
N1404	20.99	16.983	12.987	20.980	0.58	0.57	0.59	3	
N1407	28.84	10.027	7.019	13.036	0.87	0.86	0.88	3	
N1550	51.10	1466.156	138.698	154.532	1.33	1.33	1.33	5	
N1553	18.54	2.812	0.200	5.423	0.41	0.40	0.42	3	
N1600	57.40	33.050	31.097	35.003	1.43	1.39	1.47	7	
N1700	44.26	9.691	9.306	10.076	0.43	0.42	0.44	7	
N2300	30.40	14.442	12.292	22.890	0.62	0.48	0.69	6	
N2563	67.80	70.908	66.974	74.842	1.48	1.44	1.52	7	
N3115	9.68	0.025	0.020	0.032	0.44	0.34	0.60	2	
N3379	10.57	0.044	0.037	0.050	0.25	0.23	0.27	1	
N3402	60.40	512.093	488.816	535.370	0.96	0.94	0.98	4	
N3607	22.80	1.688	1.494	1.882	0.59	0.52	0.66	1	
N3608	22.91	0.437	0.367	0.507	0.40	0.34	0.49	1	
N3842	97.00	7.977	6.878	9.076	1.04	1.00	1.08	7	[a]
N3923	22.91	4.410	4.346	4.474	0.45	0.44	0.46	2	
N4104	120.00	470.995	468.941	473.049	1.52	1.47	1.57	8	
N4125	23.88	3.180	3.126	3.235	0.41	0.40	0.42	2	
N4261	31.62	7.213	7.098	7.327	0.76	0.75	0.77	1	
N4278	16.07	0.260	0.246	0.274	0.30	0.29	0.31	1	
N4291	26.18	8.021	7.660	20.148	0.59	0.52	0.65	6	
N4325	110.00	1257.102	1188.887	1325.317	1.00	0.99	1.01	4	
N4342	16.50	0.164	0.151	0.178	0.59	0.55	0.64	1	
N4374	18.37	6.556	5.397	7.716	0.73	0.73	0.74	1	
N4382	18.45	1.040	1.003	1.077	0.39	0.37	0.40	1	
N4406	17.14	132.997	131.808	134.185	0.82	0.81	0.83	1	
N4438	18.00	2.807	2.565	3.049	0.83	0.80	0.86	7	
N4472	16.29	21.982	20.186	23.778	0.95	0.94	0.96	1	
N4477	16.50	0.926	0.887	0.964	0.33	0.32	0.34	1	
N4526	16.90	0.298	0.278	0.317	0.31	0.29	0.32	1	
N4552	15.35	2.033	1.951	2.115	0.59	0.59	0.60	1	
N4555	91.50	51.000	48.512	53.488	1.00	0.98	1.02	7	
N4594	9.77	0.752	0.705	0.799	0.46	0.45	0.47	7	
N4636	14.66	33.362	32.707	34.017	0.73	0.72	0.73	1	
N4649	16.83	17.238	15.781	18.696	0.86	0.86	0.86	1	
N4782	60.00	24.721	22.583	26.859	1.15	1.11	1.19	7	
N5044	31.19	259.833	179.884	339.782	0.91	0.90	0.92	3	
N5129	103.00	397.846	32.981	46.587	0.81	0.80	0.82	5	
N5171	100.00	59.950	56.812	63.088	0.86	0.84	0.88	7	
N5813	32.21	74.822	74.461	75.167	0.70	0.69	0.70	1	
N5846	24.89	53.434	52.264	54.603	0.72	0.72	0.73	1	
N5866	15.35	0.267	0.245	0.289	0.32	0.30	0.34	1	
N6107	127.90	1512.000	1391.000	1633.000	1.86	1.69	2.03	8	
N6338	123.03	2711.934	2291.479	3132.389	1.97	1.88	2.06	4	

Table 6
(Continued)

Name	d	$L_{X,GAS}$	Lxgas_lo	Lxgas_up	T_{GAS}	Tgas_lo	Tgas_up	References	Note
N6482	58.40	167.126	39.323	294.928	0.74	0.73	0.75	3	
N6861	28.05	19.768	19.345	20.190	1.08	1.07	1.09	7	
N6868	26.79	20.414	20.049	20.780	0.69	0.68	0.70	7	
N7618	74.00	211.327	128.634	294.021	0.80	0.79	0.81	3	
N7619	52.97	77.939	12.352	155.509	0.81	0.78	0.84	6	
N7626	56.00	14.096	12.519	15.673	0.79	0.74	0.84	7	[a]

Notes. $L_{X,GAS}$: X-ray luminosity in 10^{40} erg s^{-1} of the entire hot gas. Lxgas_lo: Lower bound of $L_{X,GAS}$. Lxgas_up: upper bound of $L_{X,GAS}$. T_{GAS} in keV: tempeature of the hot gas (determined by fitting a single spectrum extracted from the entire hot gas). Tgas_lo: lower bound of T_{GAS}. Tgas_up: upper bound of T_{GAS}.
[a] Gas properties are measured within limited radii because of nearby sources. N1387 $r < 2$ Re (inside the Fornax cluster). N3842 $r < 1$ Re (embedded in a cluster). N7626 $r < 5$ Re (inside the N7619 group).
References. (1) Kim & Fabbiano (2015). (2) Boroson et al. (2011). (3) Diehl & Statler (2008b). (4) Lovisari et al. (2015). (5) Eckmiller et al. (2011). (6) O'Sullivan et al. (2003). (7) This work. (8) O'Sullivan et al. (2001).

have been extensively used to understand the stellar populations of ETGs via X-ray luminosity functions (XLFs; e.g., Figure 4 in Kim & Fabbiano 2010) and their connections to GCs (Kundu et al. 2002; Sarazin et al. 2003), to merger histories (D'Abrusco et al. 2014), and to the age of stellar populations (Kim & Fabbiano 2010; Zhang et al. 2012). Vrtilek & Boroson (2013) have developed a new method using CCI color–color-intensity (CCI) maps that have proved to be particularly apt when used with the *Chandra* data in order to separate different types of X-ray point sources. We will apply a similar method to our ETG sample and further compare the sample of starburst galaxies (N. Islam et al. 2109, in preparation).

5.6. Planned Works

We plan to add the following in the next version.

1. New galaxies. We will continue to add new galaxies and will post the same type of data products on the CGA website.
2. Fe map. The metal abundance measurement is reliable only for data with high S/N. We will add the Fe maps of a limited sample of hot gas-rich systems.
3. Circum-nuclear region. We will apply the sub-pixel resolution algorithm to produce high-resolution images in a special region of interest.
4. *XMM-Newton* data. We will further extend our program by adding *XMM-Newton* data to allow us to trace the full extent of hot gas halos. With the higher effective area and larger field of view of *XMM-Newton*, we will be able to adequately investigate the faint diffuse emission in the galaxy outskirts, which are critical to understand the interaction with the surrounding medium (e.g., by ram pressure stripping) and neighboring galaxies (sloshing, merging), to measure the hot gas properties and mass profile on as large a scale as possible.

Appendix A
CGA Data Products

The following downloadable data products are made available in two packages. The main package (package 1) consists of the high-level data products, e.g., point-source-removed and filled exposure-corrected images (jpg/png and FITS format) in multiple energy bands to best illustrate the diffuse hot gas distribution, and derived T-maps (jpg/png and FITS format) in various adaptive binning methods to show the hot gas thermal structure. They can be used directly for an overview, to obtain the necessary hot gas quantities, and to compare them with data at other wavelengths with no additional X-ray data reduction.

For those who intend to perform their own analyses, e.g., to extract and fit X-ray spectra from user-specified regions, we provide all the necessary data in the supplementary package (package 2), e.g., event files for each obsid and for each ccd.

Data in **bold** letters below are in the main package, and the others are in the supplementary package. Data in *italic* letters are not in the package because of the large number of files and their size. They can be made available upon request.

Merged data (see Section 3.1).

1. ${gmv}$_evt.fits—a single event file containing the entire observations of a given galaxy. Here g, m, and v in ${gmv}$ indicate galaxy name, merge id (mid), and version. ${gmv}$ looks like N1234_90201_v01.
2. **${gmve}$_img.fits**—a full-resolution image for a given energy band. One pixel corresponds to 0.492 arcsec. Here e in ${gmve}$ indicates an energy band (a short name in Table 3). ${gmve}$ looks like N1234_90201_v01_G.
3. **${gmve}$_exp.fits**—a matching exposure map for a given energy band in unit of cm^2 s (=effective area × exposure time). Due to the energy dependent effective area, the exposure map was made at the effective energy for each energy band given in Table 3.
4. ${gmv}$_frame.reg—an ASCII region file of the full field of view. It contains one polygon for each obsid in a physical pixel coordinate.

5. ${gmv}_frame_fk5.reg—same as the above, but in fk5 (in sexagesimal).

Point-source list (see Section 3.2).

1. ${gmve}_src.fits—a source list (FITS table) for each energy band. They were detected by wavdetect in the merged image file.
2. ${gmv}_src_psfsize.fits—a list of sources in a FITS file that are to be removed. To avoid false sources to be excluded, we limit sources with net counts >10 and significance $>3\sigma$. As described in Section 3.2, the sources are determined in the C-band detections by default, but when the diffuse emission is strong in the central region of gas-rich galaxies, the sources are instead determined in the H-band detections. The source sizes (used to remove them) are set by MARX PSF with variable EE fractions depending on the source strength.
3. ${gmv}_src_psfsize.dat—same as above, but an ASCII list file with additional information about ra, dec, and net counts.

Event and image files after point sources are removed (not filled).

1. ${gmv}_psrem.evt—an event file containing all data for all obsids and all ccds. All detected point sources were removed, but not filled.
2. ${gmv}_C_psrem.img—an image file containing data for all obsids and all ccds for the C energy band. All detected point sources were removed, but not filled. This image file is used in the 2D adaptive binning (Section 3.3).
3. ${gmv}_${oc}_psrem_evt.fits—a FITS event file for each obsid for each ccd. They are used for spectral extraction of each binned region. (Section 3.4).
4. ${gmv}_${oc}_psrem_bevt.fits—corresponding background FITS event file for each obsid for each ccd. They were made appropriate for each obsid from the blank-sky data (Section 3.4).

Diffuse images after point sources are removed and filled (see Section 3.2).

1. ${gmve}_diff_img.fits—a diffuse image for a given energy band. This image was made after point sources were removed and holes were filled by surrounding pixels.
2. ${gmve}_diff_flux.fits—an exposure-corrected, flux-diffuse image for a given energy band. It was made from a diffuse image divided by a corresponding exposure map.
3. ${gmve}_sm_diff_img.fits—a smoothed diffuse image for a given energy band by the 2D Gaussian smoothing with a 5σ kernel (7 pixels per σ) was applied.
4. ${gmve}_sm_diff_flux.fits—a smoothed, exposure-corrected flux-diffuse image for a given energy band. The same smoothing was applied as in the above.

JPEG/PNG figures of the above images

1. ${gmve}_img_${z}.jpg—a ds9 jpg file for an X-ray image, ${gmve}_img. Here ${z} indicates a zoom factor (z1 = unzoomed, z05 = zoomed out by a factor of 1/2).
2. ${gmve}_exp_${z}.jpg—a ds9 jpg file for an exposure map, ${gmve}_exp.

3. ${gmve}_flux_${z}.jpg—a ds9 jpg file for a flux image, ${gmve}_flux.
4. ${gmv}_rgb.png—three color images to visualize the 2D spectral variation (including point sources). The energy bands used in rgb are 0.5–1.2, 1.2–2, and 2–7 keV, respectively.
5. ${gm}_OX.png—a ds9 jpg file to compare the X-ray (${gmve}.img where $e = B$ band) and optical (DSS POSS2 Red) images. The D_{25} ellipse (from RC3) and the FOV (${gmv}_frame.reg) are overlaid.
6. ${gmve}_diff_img_${z}.jpg—a ds9 jpg file for a diffuse image, ${gmve}_diff.img.
7. ${gmve}_diff_flux_${z}.jpg—a ds9 jpg file for a diffuse flux image, ${gmve}_diff.flux.
8. ${gmve}_sm_diff_img_${z}.jpg—a ds9 jpg file for a smoothed diffuse image, ${gmve}_sm_diff.img.
9. ${gmve}_sm_diff_flux_${z}.jpg—a ds9 jpg file for a smoothed diffuse flux image, ${gmve}_sm_diff.flux.

Adaptively binned spatial regions and images (see Section 3.3).

1. ${gmvb}_Imap.fits—a FITS image with pixel value = relative intensity in each bin. Here b in in the filename indicates one of four binning methods (AB, WB, CB, and HB). ${gmvb} is like N1234_90201_v01_WB.
2. ${gmvbn}.reg—an ASCII region file for the nth bin. Here n in in the filename is a five-digit bin number. ${gmvbn} is like N1234_90201_v01_WB_00012.
3. ${gmvb}_binno.fits—a FITS image file with pixel value = bin number.
4. ${gmvb}_binrad.fits—a FITS image file with pixel value = radius of bin (only for HB). Due to the nature of the HB method, the spectral extraction region is different from the bin and the extraction circle is generally overlapping and larger than the bin size given by the square grid.

Spectra, arf, and rmf for each bin (see Section 3.4).

1. ${gmvbn}.pi—A type I PHA file for the source spectrum for the nth bin, extracted from individual event files for each obsid and for each ccd, then combined into a single file (see Section 3.4).
2. ${gmvbn}_bkg.pi—same as the above, but for the background spectrum. The same extraction region is used as in the source spectrum.
3. ${gmvbn}_src.arf—an ancilliary response file (ARF) for the nth bin, made for each obsid and for each ccd, then combined into a single file.
4. ${gmvbn}_src.rmf—an response matrix file (RMF) for the nth bin, made for each obsid and for each ccd, then combined into a single file.

Fitting results (see Section 3.4).

1. ${gmvb}_sum.dat—an ASCII table containing (1) bin number, (2) galactocentric distance in arcminutes determined by photon-weighted mean distance from the galaxy center, (3) area of the bin in pixels (one ACIS pixel is $0''.492 \times 0''.492$) (4–5) total and net counts, (6) reduced χ^2, (7–9) best-fit T and its 1σ lower and upper bounds, (10) T error in percent, (11–13) APEC

normalization parameter divided by bin area and its 1σ lower and upper bounds.

2. ${gmvbns}.log—an ASCII log file for SHERPA spectral fitting. Here, s in ${gmvbns} indicates spectral models (e.g., APEC, APECnPL = APEC + power-law). ${gmvbns} looks like N1234_90201_v01_WB_00012_APECnPL.

Spectral maps (see Section 3.4).

1. ${gmvbsp}map.fits—A FITS image with pixel value = spectral parameter. Here p in the filename indicates the spectral parameters used in the map (T = temperarure, N = norm of the APEC component/area of the bin, P = projected pseudo-pressure and K = projected pseudo-entropy). ${gmvbsp} is like N1234_90201_v01_WB_A-PECnPL_T. The T map is in keV unit and the other maps are in arbitrary units (see Section 3.5).

2. ${gmvbsp}map_lo.fits—same as the above, but with pixel value = lower limit of a given parameter.

3. ${gmvbsp}map_up.fits—same as the above, but with pixel value = upper limit of a given parameter.

4. **${gmvbsp}map_30pc.fits**—same as ${gmvbsp}.map, but the bins with a large error (>30% in T) are masked out. Here ${gmvbrsp} looks like N1234_90201_v01_WB_sn20_APECnPL_T.

5. **${gmvbs}_Cmap_30pc.fits**—A FITS image with pixel value = reduced chi2.

PNG figures

1. **${gmbr}_Imap.png**—a png file of the binned intensity map, ${gmvb}_Imap.fits.

2. **${gmbrsp}map.png**—a png file of the masked (by 30% T error) spectral parameter maps, ${gmvbsp} map_30pc.fits.

3. **${gmvbs}_Cmap.png**—a png file with pixel value = reduced chi2.

Appendix B
Notes on Individual Galaxies

Based on the 1D radial profiles and 2D spectral maps, we describe important features of individual galaxies. We also include the distinct features previously known by targeted studies. We use the terms surface brightness (SB), temperature (T), emission measure (EM), projected or pseudo-pressure (P) and projected or pseudo-entropy (K). In describing temperature profiles, we call the case with a negative T gradient in the central region (roughly within a few kpc or $\sim$0.5 r_e) a hot core and the case with a positive T gradient in the central region a cool core.

IC 1262 ($d = 130.0$ Mpc, $1' = 37.8$ kpc, $r_e = 7.7$ kpc, $r_{25} = 22.7$ kpc). This is a dominant galaxy in a small group. While the hot gas halo is roughly symmetric and smooth on a large scale (>100 kpc), the hot ISM on a smaller scale exhibits rather complex substructures: a sharp discontinuity to the E and narrow arcs over 100 kpc long in the NS direction (Trinchieri et al. 2007). Also detected are cavities at 10–20 kpc to the N (Dong et al. 2010). The hot gas in the enhanced surface brightness regions to the E from the center in $r < 20$ kpc ($\sim$1 keV) and to the NS in $r = 20$–100 kpc ($\sim$1.2 keV) is cooler than the surrounding gas ($\sim$1.6 keV). The gas thermal

structures are also visible in the entropy map: the lowest entropy gas is extended to the E, the lower entropy gas is extended to the NS, surrounded by the higher entropy gas.

IC 1459 ($d = 29.2$ Mpc, $1' = 8.5$ kpc, $r_e = 5.2$ kpc, $r_{25} = 22.3$ kpc). This is a dominant galaxy in a small group. A strong nuclear source ($L_X = 8 \times 10^{40}$ erg s^{-1}) dominates the X-ray emission (Fabbiano et al. 2003). Because of the strong central source, there are (weak) ACIS readout streaks along the CCD column, visible in the smoothed diffuse image. Note that they are not excluded in this image, but the streak regions were excluded in the spectral analysis (see Section 4.3). The faint diffuse gas is extended to fill the D$_{25}$ ellipse. While the surface brightness is azimuthally symmetric, the 2D temperatures map shows slight asymmetry in that the gas along the minor axis (0.6–0.7 keV) is hotter than that along the major axis (0.4–0.5 keV).

IC 1860 ($d = 93.8$ Mpc, $1' = 27.3$ kpc, $r_e = 8.4$ kpc, $r_{25} = 23.7$ kpc). This is the BCG (brightest cluster galaxy) of AS301. It has previously been known to be sloshing (Gastaldello et al. 2013). The intensity and temperature maps show a narrow tail, extending to $r = 1'$ (or 27 kpc) toward the SE direction from the core. The gas in the tail is cooler ($\sim$1 kev) than that in the surrounding region (1.3 keV). The tail is also visible in the projected entropy map, but not obviously clear in the projected pressure map, indicating the pressure balance with the surrounding medium. Excluding the tail, the hot gas emission on a large scale (at or outside the D$_{25}$ ellipse) is more pronounced toward the SW and relatively weaker toward the NE direction.

IC 4296 ($d = 50.8$ Mpc, $1' = 14.8$ kpc, $r_e = 11.9$ kpc, $r_{25} = 25.0$ kpc). This is the BCG in A3565. A strong nuclear source ($L_X = 2.4 \times 10^{41}$ erg s^{-1}) dominates the X-ray emission (Pellegrini et al. 2003; Humphrey & Buote 2006). The hot gas distribution is asymmetric, mainly extending to $r = 1'.6$ or 20 kpc toward the SW direction in a fan-shape (PA = 280°–350°). The gas temperature in that region is hotter ($\sim$1.3 keV) than that in the central region (0.8 keV). The ACIS observation was msde in a subarray mode with 512 rows, but the entire D25 ellipse is included. A nearby spiral galaxy, IC 4299, which is at 6′.2 to the S of IC 4296, is also detected just inside the field of view (FOV).

NGC 193 ($d = 47.0$ Mpc, $1' = 13.7$ kpc, $r_e = 4.4$ kpc, $r_{25} = 9.9$ kpc). This is a FR-I radio galaxy (Laing et al. 2011). The hot gas exhibits a well-structured shell at $r = 1'$–1′.5 (or 14–20 kpc). The radio lobes have inflated into a cocoon or a large cavity and the shell of shocked material around the cavity (Bogdan et al. 2014). The gas in the cavity is cooler ($\sim$0.7 keV) than that in the shell ($\sim$1 keV). It also has a distinct X-ray point source at the center.

NGC 315 ($d = 69.8$ Mpc, $1' = 20.3$ kpc, $r_e = 12.5$ kpc, $r_{25} = 32.9$ kpc). This is a FR-I radio galaxy. The *Chandra* observations reveal a strong nuclear X-ray source ($L_X = 5 \times 10^{41}$ erg s^{-1}) and also an X-ray jet ($\Gamma_{PH} \sim 2.2$) extending to $r = 1'$ (or 20 kpc), coincident with an NW radio jet (Worrall et al. 2003, 2007). The strong nucleus causes (weak) CCD readout streaks along the CCD column, which are visible in the diffuse image. Note that they are not excluded in this image, but the streak regions were excluded in the spectral analysis (see Section 4.3).

Table 7
Nearby Galaxies of NGC 383

Name	R.A. (J2000)	Decl. (J2000)	$D(')$ From N383	PA(degree) From N383
NGC 375	16.77466	32.34817	5.'6	226
NGC 379	16.81537	32.52036	6.'8	343
NGC 380	16.82330	32.48292	4.'5	340
NGC 382	16.84946	32.40386	0.'6	200
NGC 384	16.85460	32.29245	7.'2	180
NGC 385	16.86352	32.31953	5.'6	175
NGC 386	16.88039	32.36199	3.'3	156
NGC 387	16.88775	32.39111	2.'2	127

NGC 383 ($d = 63.4$ Mpc, $1' = 18.4$ kpc, $r_e = 6.3$ kpc, $r_{25} = 14.6$ kpc). This is a FR-I radio galaxy (3C 31). The *Chandra* observations reveal a strong nuclear X-ray source (several $\times 10^{41}$ erg s^{-1}) and also an X-ray jet extending to $r = 10''$ or 3 kpc, coincident with the brighter, northern radio jet of 3C 31 (Hardcastle et al. 2002). Because of its small scale, the northern jet is only seen in the unsmoothed image. A nearby galaxy, NGC 382, lying inside the D25 ellipse at ~0.'6 S (PA = 200°) from NGC 383, is also detected with a similar gas temperature (~0.7 keV). A few nearby galaxies of the Arp 331 chain (Table 7) are also detected in the ACIS FOV. See Table 7 for the list of nearby galaxies.

NGC 499 ($d = 54.45$ Mpc, $1' = 15.8$ kpc, $r_e = 4.4$ kpc, $r_{25} = 12.8$ kpc). This is the second brightest galaxy in the NGC 507 group (13.'7 to the NW, PA = 334° from NGC 507). Given its high $L_{X,GAS}$ ($>10^{42}$ erg s^{-1}) and T_{GAS} (~1 keV at the outskirts), it is likely a separate group that is currently merging with the NGC 507 group. NGC 499 and NGC 507 belong to one group in the 2MASS group catalog (Crook et al. 2007), but they are identified as two separate groups in the Lyon group catalog (Garcia 1993). The temperature radial profile is a typical case with a hot core. In contrast to a cool core, the T gradient is negative in the inner region ($r < 10$ kpc) and positive in the outer region ($r > 10$ kpc). Although at the outskirts ($r > 70$ kpc) the temperature (as well as the surface brightness) increases with increasing radius because the ICM of the NGC 507 group is hotter, the inner temperature profile is not affected by the ICM and therefore intrinsic to NGC 499. The 2D temperature map further shows that the gas distribution is azimuthally asymmetric. The inner hotter gas (~0.85 keV) extending to $r = 20''$ or 5 kpc is elongated along the major axis (PA = 70°), while the outer cooler gas (~0.65 keV), extending to $r = 2'$ or 30 kpc, is elongated along the NE-SW direction (PA ~ 40°). There are two possible ghost cavities just outside the D25 ellipse (at $r = 10$–15 kpc), one to the N (PA ~ 20°) and another to the S (PA ~ 160°) from the galaxy center, seen in the diffuse image as well as in the projected pressure map. It is likely that all these features suggest past, multiple AGN activities.

NGC 507 ($d = 63.8$ Mpc, $1' = 18.6$ kpc, $r_e = 12.9$ kpc, $r_{25} = 28.7$ kpc). This is the BCG in an optically rich group, merging with NGC 499 (at 13.'7 to the NW, PA = 334). The T profile indicates the presence of a cool core and the SB profile shows the central cusp. The 2D maps illustrate rather complex substructures. Its core region has cavities, possibly related to the old bent radio lobes (Giacintucci et al. 2011). Kraft et al. (2004) identified an abundance front. The hot gas is probably sloshing owing to interaction with NGC 499. NGC 508 at ~1.'5 to the N is also detected in the same observation.

Table 8
Nearby Galaxies of NGC 741

Name	R.A. (J2000)	Decl. (J2000)	$D(')$ From N741	PA(deg) From N741	Other Names
NGC 742	29.10072	5.62668	0.'8	100	
ARK 065	29.05004	5.58858	3.'3	223	P007237
ARK 066	29.07938	5.65208	1.'5	341	P007250 IC 1751

NGC 533 ($d = 76.9$ Mpc, $1' = 22.4$ kpc, $r_e = 16.2$ kpc, $r_{25} = 42.5$ kpc). This is a relaxed group with a cool core (Eckmiller et al. 2011; Panagoulia et al. 2014). The T profile shows cooler gas ($T \sim 0.8$ keV) in the inner region ($r < 5$ kpc). The temperature steeply rises to ~1.3 keV at $r = 16$ kpc (close to r_e), then remains constant to $r = 80$ kpc (~5 r_e). The T map further indicates an asymmetric cool core. Inside $r = 20$ kpc, the hot gas is distributed along the major axis, generally following the optical light distribution (ellipticity $e = 0.4$). This is most clearly seen in the T and projected entropy maps, possibly indicating sloshing by a nearby galaxy. In the outer region ($r = 20$–60 kpc), the hot gas is more extended to the N and NE than toward the S. Note that the lower SB region just inside the D$_{25}$ ellipse to the S is affected by the node boundary, which is not fully corrected even in the exposure-corrected diffuse emission map. However, the lower SB region outside the D$_{25}$ ellipse toward the S is not affected. Shin et al. (2016) found two cavities at 1.5 kpc N and S of the nucleus. There is a possible ghost cavity at $r \sim 5$ kpc from the center toward the NW.

NGC 720 ($d = 27.7$ Mpc, $1' = 8.0$ kpc, $r_e = 4.8$ kpc, $r_{25} = 18.8$ kpc). This system was extensively studied as a relaxed system where mass can be measured accurately (Buote et al. 2002 and Humphrey et al. 2011). The T profile and T map both show more or less constant T (~0.6 keV) throughout the galaxy ($r = 2$–20 kpc) with hints of increasing T toward the center and decreasing T at the outskirts. Unlike NGC 533, the gas distribution is considerably rounder than the optical figure ($e = 0.5$), as seen in the intensity map as well as in the projected pressure and entropy maps.

NGC 741 ($d = 70.9$ Mpc, $1' = 20.6$ kpc, $r_e = 13.2$ kpc, $r_{25} = 30.4$ kpc). This is a disturbed system, owing to an NAT radio galaxy (PKS 0153+05) and NGC 742 (at 0.'8 to the E) falling through the core. Jetha et al. (2008) reported complex gas structures with X-ray filaments linking NGC 741 and NGC 742 and a possible ghost cavity to the W of NGC 741 (see also Schellenberger et al. 2017). Even if it is not relaxed, NGC 741 has a cool core (~0.7 keV) and hotter gas (1.2 keV) at the outskirts. NGC 742 has a nuclear X-ray source at the center that dominates its entire X-ray emission. Also detected in the ACIS FOV are two compact galaxies, ARK065 and ARK066, at a similar redshift as NGC 741 and 742. See Table 8 for the list of nearby galaxies.

NGC 1052 ($d = 19.4$ Mpc, $1' = 5.6$ kpc, $r_e = 3.1$ kpc, $r_{25} = 8.5$ kpc). This is a well-known LINER. A variable nuclear X-ray source dominates the entire X-ray emission (Hernández-García et al. 2013). Soft (0.4 keV) diffuse gas emission is seen inside a few kiloparsec from the center. Asymmetric T maps (0.4 keV to the E and 0.7 keV to the W) seen in WB and HB need to be confirmed by deeper observations.

NGC 1132 ($d = 95.0$ Mpc, $1' = 27.6$ kpc, $r_e = 15.5$ kpc, $r_{25} = 34.7$ kpc). This is a fossil group with an extended, luminous X-ray halo ($L_X \sim 7 \times 10^{42}$ erg s^{-1}, Lovisari et al.

2015). The T profile shows a cool core ($\sim$0.8 keV). The azimuthally averaged temperature peaks at $\sim$10 kpc (1.3 keV) and declines outward to $\sim$1 keV. In contrast to the expectation as a fossil system, the hot gas morphology indicates asymmetry, an edge to the E, and extended emission to the W, possibly implying a rare case of a rejuvenated fossil group (e.g., von Benda-Beckmann et al. 2008). The detailed observational results and implications are presented in a separate paper (Kim et al. 2018).

NGC 1316 ($d = 21.5$ Mpc, $1' = 6.2$ kpc, $r_e = 7.6$ kpc, $r_{25} = 37.6$ kpc). This is a radio galaxy (Fornax A) with radio jets and extended lobes in the E-W direction (Ekers et al. 1983) and exhibits a number of signs of recent major mergers 2–3 Gyr ago (Schweizer 1980). The hot gas morphology also indicates a disturbed nature and cavities associated with the radio jets (Kim & Fabbiano 2003). Given the high optical luminosity and size of the stellar system, the amount ($L_{X,GAS} \sim$ a few $\times 10^{40}$ erg s^{-1}) and the extent ($\sim$10 kpc) of hot gas are very low, making its L_X/L_K one of the lowest of nearby ETGs. The azimuthally averaged temperature decreases from the center to $r \sim 10$ kpc, then increases outward to 20 kpc. The SB and temperature maps indicate that the gas is not symmetric, however.

NGC 1332 ($d = 22.9$ Mpc, $1' = 6.7$ kpc, $r_e = 3.1$ kpc, $r_{25} = 15.6$ kpc). This is an edge-on S0 galaxy. The temperature is almost constant at 0.6 keV inside the D25 ellipse, but the hot gas may be slightly hotter ($\sim$0.7 keV) in the central region.

NGC 1380 ($d = 17.6$ Mpc, $1' = 5.1$ kpc, $r_e = 3.2$ kpc, $r_{25} = 12.3$ kpc). This is an edge-on S0 galaxy in the Fornax cluster. It is located at $37.'8$ to the NW from NGC 1399. The hot ISM ($\sim$0.3 keV) is detected but confined within a few kiloparsec ($\sim$1 r_e). The hotter (1.2–1.5 keV) ICM in the Fornax cluster is also detected at $r > 10$ kpc.

NGC 1387 ($d = 20.3$ Mpc, $1' = 5.9$ kpc, $r_e = 3.5$ kpc, $r_{25} = 8.3$ kpc). This is a barred S0 (SB0) galaxy in the Fornax cluster. It is located at $19'$ to the W (PA = 260) from NGC 1399. The hot ISM ($\sim$0.5 keV) is detected but confined within several kpc (or $\sim$2 r_e). The hotter (1.2–1.5 keV) ICM in the Fornax cluster is also detected at $r > 10$ kpc. Note that the X-ray bright part is on the ACIS-I chip gap, although the exposure map appears to work properly.

NGC 1395 ($d = 24.1$ Mpc, $1' = 7.0$ kpc, $r_e = 5.4$ kpc, $r_{25} = 20.6$ kpc). This is a large elliptical galaxy ($M_K = -25$ mag), and the hot gas temperature is comparably high (0.8–0.9 keV). Given the short *Chandra* observations with significant background flares, the hot gas is limited roughly within the D25 ellipse, and its temperature is more or less constant.

NGC 1399 ($d = 20.0$ Mpc, $1' = 5.8$ kpc, $r_e = 4.7$ kpc, $r_{25} = 20.1$ kpc). This is at the center of the Fornax cluster and contains a large amount of extended hot halo. Although NGC 1316 ($3.°6$ away in projection) is optically brighter by a factor of two (hence BGC), NGC 1399 is at the bottom of the potential well. On a galaxy scale (inside the D25 ellipse), the intensity maps show two filaments to the north and one to the south. The radio jets are propagating between the two northern filaments and at the side along the southern filament (Paolillo et al. 2002 and Werner et al. 2012). The T maps show the cooler gas (0.8–1 keV) extending in the N-S direction along the filaments. The projected pressure map also shows the gaps where the radio jets are propagating. On a large cluster scale, the *Chandra* observations of the Fornax cluster (3×3 ACIS-I

observations) reveal the asymmetric intracluster gas (Scharf et al. 2005). The hot halo is extended to $r \sim 30'$ (180 kpc) to the NE of NGC 1399. A few discontinuities, likely due to sloshing, are also detected by Su et al. (2017b).

NGC 1400 ($d = 26.4$ Mpc, $1' = 7.7$ kpc, $r_e = 2.9$ kpc, $r_{25} = 8.8$ kpc). This is a member of the NGC 1407/NGC 1400 merging group, $12'$ away to the SW (PA = 236°) from NGC 1407. Note that the galaxy (the NW side) is not fully covered by the deeper of two observations. The hot ISM (0.5–0.6 keV) is confined inside the D$_{25}$ ellipse and surrounded by the hotter ambient gas ($\sim$1.2 keV) at $r > 20$ kpc. There is also a blob of hot gas at $3'$–$5'$ away to the NE from NGC 1400 (Giacintucci et al. 2012; Su et al. 2014). Because the external hot gas has a similar temperature and abundance to that of NGC 1400, Su et al. (2014) suggested that it might have come out of NGC 1400 by ram pressure stripping.

NGC 1404 ($d = 21.0$ Mpc, $1' = 6.1$ kpc, $r_e = 2.7$ kpc, $r_{25} = 10.1$ kpc). This is a member of the Fornax cluster, only $10'$ (in projection 60 kpc) away to the SE (PA = 152°) from NGC 1399. It is one of the most extensively studied ETGs due to a sharp discontinuity to the direction of NGC 1399 (Machacek et al. 2005; Su et al. 2017a). The *Chandra* observations reveal a front at the NW edge and a tail to the SE, indicating that it is currently falling through the Fornax cluster. The temperature radial profile indicates a hot core as in the case of NGC 499. The temperature is 0.8 keV at the central region and decreases to 0.5 keV at $r = 4$ kpc (just outside r_e) and steeply rises at $r = 5$–20 kpc to 1.3 keV. In the 2D spectral maps, the head-tail structure is clearly visible.

NGC 1407 ($d = 28.8$ Mpc, $1' = 8.4$ kpc, $r_e = 8.9$ kpc, $r_{25} = 19.2$ kpc). This is the BCG in a small group. It has a cool core with an edge to the N (at $r = 7$–8 kpc) and wings extending to the E-W, suggesting that the galaxy is moving to the N direction. The wings are inside a large-scale old diffuse radio structure, and they are bent, likely as a consequence of motion to the N (Giacintucci et al. 2012). The temperature radial profile indicates another hot core case: T is $\sim$1 keV in the center, decreases to $\sim$0.8 keV at $r = 1$–3 kpc, then rises to $\sim$1.3 keV at the outskirts ($r > 20$ kpc). The temperature maps further reveal that the cooler E-W wings extend to beyond the D$_{25}$ ellipse.

NGC 1550 ($d = 51.1$ Mpc, $1' = 14.9$ kpc, $r_e = 6.3$ kpc, $r_{25} = 16.6$ kpc). This is the dominant galaxy in a group. This group is one of the most luminous local groups with $L_X \sim 10^{43}$ erg s^{-1} within 200 kpc (Sun et al. 2003). On a large scale, the hot gaseous halo is smooth and circularly symmetric, as seen in the *XMM-Newton* observations (Kawaharada et al. 2009), but the central region is highly elongated. The 2D temperature map further suggests an asymmetric distribution of cooler gas ($\sim$1 keV) with a strong E-W elongation, which is more pronounced to the W. A similar trend is also seen in the projected entropy map but is not seen in the projected pressure map, indicating pressure balance between the cooler/low-entropy and hotter/high-entropy gas. The temperature radial profile shows that the temperature is constant at $\sim$1 keV within $r < 5$ kpc and rises to $\sim$1.5 keV at $r \sim 30$ kpc, then declines at the outskirts. Note that the CCD boundary of one of the two long ACIS-S observations falls at the southern end of the D$_{25}$ ellipse. While the boundary is clearly visible in the raw and binned images, it is properly treated in spectral fitting so that the spectral maps are smooth across the boundary.

NGC 1553 ($d = 18.5$ Mpc, $1' = 5.4$ kpc, $r_{\rm e} = 5.1$ kpc, $r_{25} = 12.0$ kpc). This is a face-on SB0 galaxy. A hard X-ray source ($L_{\rm X} \sim 10^{40}$ erg s^{-1}) is present at the nucleus, and the diffuse hot gas ($\sim$0.4 keV) roughly fills the D$_{25}$ ellipse. The gas emission is not smooth, the SB radial profile is rather flat, and spiral-arm-like features starting from the center are seen along the minor axis (see also Blanton et al. 2001). A deeper observation is necessary to confirm the distribution and its thermal structure of the hot gas.

NGC 1600 ($d = 57.4$ Mpc, $1' = 16.7$ kpc, $r_{\rm e} = 13.5$ kpc, $r_{25} = 20.5$ kpc). This is either a BCG in a loose group or an isolated elliptical galaxy surrounded by a number of satellite galaxies (Smith et al. 2008). Due to its low X-ray luminosity (a few $\times 10^{41}$ erg s^{-1}), it is not identified as a fossil group. It hosts a massive BH of $1.7 \times 10^{10} M_{\odot}$ (Thomas et al. 2016). The temperature profile is a typical one with a cool core. The cool core is at $T \sim 0.8$ keV and T reaches a peak ($T \sim 1.5$ keV) at a few $r_{\rm e}$, then declines outward. Also detected in X-rays are NGC 1603 ($2\rlap{.}'5$ E of NGC 1600) and NGC 1601 ($1\rlap{.}'6$ N of NGC 1600). The hot gas in NGC 1603 shows a tail to the W, due to the ram pressure from the group halo as the galaxy is moving to the E (Sivakoff et al. 2004). There is no clear signature of sloshing in the main halo, likely because NGC 1603 is too small to perturb the hot halo of the main galaxy as $\Delta m_{\rm B} = 2.7$.

NGC 1700 ($d = 44.3$ Mpc, $1' = 12.9$ kpc, $r_{\rm e} = 3.86$ kpc, $r_{25} = 21.4$ kpc). This is a giant ($M_{\rm K} = -25.5$) elliptical galaxy. A hard X-ray source ($L_{\rm X} \sim$ a few $\times 10^{40}$ erg s^{-1}) is present at the nucleus, and the diffuse hot gas ($\sim$0.5 keV) roughly fills the D$_{25}$ ellipse. The hot gas distribution is significantly flattened, likely due to the rotation, consistent with the stellar figure (E4) and kinematics (Statler & McNamara 2002). The temperature radial profile indicates a mild negative gradient (from 0.55 to 0.35 keV).

NGC 2300 ($d = 30.4$ Mpc, $1' = 8.8$ kpc, $r_{\rm e} = 4.8$ kpc, $r_{25} = 12.5$ kpc). This is the BCG in a group with the neighboring stripped spiral galaxy NGC 2276, which is moving to the SW at $\sim$850 km s^{-1}, and both galaxies are detected in X-rays (Rasmussen et al. 2006). The temperature profile of NGC 2300 is a typical one with a cool core. The cool core is at $\sim$0.6 keV and T reaches a peak $\sim$1 keV at a few $r_{\rm e}$, then declines outward. There may an edge to the E and NE and the diffuse gas is more extended to the SW. This may be due to sloshing by NGC 2276 (6$'$ away) after it has just passed the impact point.

NGC 2563 ($d = 67.8$ Mpc, $1' = 19.7$ kpc, $r_{\rm e} = 6.4$ kpc, $r_{25} = 20.6$ kpc). This is a dominant galaxy in a poor group with a typical cool core. The temperature is 0.8 keV near the center, peaks ($T \sim 1.7$ keV) at $r = 20$ kpc (3 $r_{\rm e}$), then declines outward. A nearby SB0 galaxy, NGC 2557, is also detected in X-rays. Rasmussen et al. (2012) studied individual group members with hot (X-rays) and cold (H I) gas to investigate the effect of ram pressure stripping and tidal interactions.

NGC 3115 ($d = 9.7$ Mpc, $1' = 2.8$ kpc, $r_{\rm e} = 1.6$ kpc, $r_{25} = 10.2$ kpc). This is an edge-on S0 galaxy with little hot gas. It is one of the gas-poor ETGs with very deep *Chandra* observation, targeted to study Bondi accretion (Wong et al. 2014; Lin et al. 2015a, 2015b). The hot gas is detected within $\sim$1 $r_{\rm e}$.

NGC 3379 ($d = 10.6$ Mpc, $1' = 3.1$ kpc, $r_{\rm e} = 2.4$ kpc, $r_{25} = 8.3$ kpc). This is a typical old E galaxy with little hot gas. It is one of the gas-poor ETGs with very deep *Chandra* observations, targeted to study a population of LMXBs

(Brassington et al. 2008, 2010). The hot gas ($T \sim 0.3$ keV) is detected within $\sim$1 $r_{\rm e}$ and its luminosity is one of the lowest ever measured from a hot phase of the ISM in genuine elliptical galaxies, as it is likely in the outflow phase (Trinchieri et al. 2008).

NGC 3402 = NGC 3411 ($d = 64.9$ Mpc, $1 = 18.9$ kpc, $r_{\rm e} = 8.8$ kpc, $r_{25} = 19.7$ kpc). This is the BCG in the small group USGC S152. While the diffuse gas appears to be relaxed, the temperature map clearly indicates a shell-like structure at 20–40 kpc with cooler gas ($\sim$0.8 keV) surrounded by inner and outer hotter gas ($\sim$1 keV), as previously reported by O'Sullivan et al. (2007). The cooler gas is most obvious in the N (PA $= -20°$–$20°$) and E (PA $= 90°$–$135°$) and least clear in the SW (PA $= 220°$–$300°$). This feature is not seen in the intensity, EM, projected pressure, and projected entropy maps. It is not understood what caused the cooler shell. The possibilities include a previous AGN activity that might reheat the cool core and settling of material stripped from the halo of one of the other group member galaxies (O'Sullivan et al. 2007).

NGC 3607 ($d = 22.8$ Mpc, $1' = 6.6$ kpc, $r_{\rm e} = 5.0$ kpc, $r_{25} = 16.2$ kpc). This is a dominant E/S0 galaxy in the small group USGC U376 in the Leo cloud (Mazzei et al. 2014) with NGC 3608 ($5\rlap{.}'9$ N) and NGC 3605 ($2\rlap{.}'7$ SW). A hot core ($\sim$1 keV) may be present in the central region ($r < 0.5$ kpc), and then the gas temperature remains constant at 0.5 keV in $r < r_{\rm e}$. The SB profile is also relatively flat ($\sim r^{-1}$) at $r = 1$–10 kpc. Given the limited statistics of the *Chandra* data, it is not clear whether the hot gas indicates any sign of interactions. Both NGC 3607 and 3608 are known to be LINERs, and the X-ray nuclear sources were studied by Flohic et al. (2006).

NGC 3608 ($d = 22.9$ Mpc, $1' = 6.7$ kpc, $r_{\rm e} = 3.3$ kpc, $r_{25} = 10.5$ kpc). This is an elliptical galaxy at $5\rlap{.}'9$ (or $\sim$40 kpc in projection) away from NGC 3607 and in the same FOV as the *Chandra* observation of NGC 3607. As it is slightly smaller than NGC 3607 (0.8 mag less bright in K band), its $L_{\rm X}$ and $T_{\rm X}$ are slightly lower. The gas temperature is constant at $\sim$0.4 keV, and the SB profile is relatively flat ($\sim r^{-1}$) at $r < 2$ $r_{\rm e}$.

NGC 3842 ($d = 97.0$ Mpc, $1' = 28.2$ kpc, $r_{\rm e} = 17.8$ kpc, $r_{25} = 19.9$ kpc). This is the BCG of A1367, but it is not at the center of the hot ICM, nor at the center of the cluster potential well. The diffuse hot gas at $T \sim 1$ keV is detected inside the D$_{25}$ ellipse. The hot ISM is embedded inside the hotter (5–6 keV) subcluster, which is merging with the primary cluster of A1367 centered at 20$'$ SE of NGC 3842 (see Sun et al. 2005; Sun & Vikhlinin 2005). A few other galaxies in the A1367 subcluster (see Table 9) are also detected in the same FOV. See Table 9 for the list of nearby galaxies.

NGC 3923 ($d = 22.9$ Mpc, $1' = 6.7$ kpc, $r_{\rm e} = 5.8$ kpc, $r_{25} = 19.6$ kpc). This is a young elliptical (E4) galaxy with a number of stellar shells (Bilek et al. 2016). The extended hot gas is detected inside the D$_{25}$ ellipse and is elongated along the major axis, but not as flat as the stellar system. In the inner region, the temperature decreases with increasing r, i.e., a hot core (0.7 keV at $r = 0.1$ kpc). T reaches at the minimum (0.4 keV) at $r = 3$ kpc, then increases again to 0.6 keV at $r = 10$–20 kpc. Kim & Fabbiano (2010) and Kim et al. (2012) investigated this galaxy in a sample of young elliptical galaxies in terms of the X-ray binary luminosity function and the hot gas metallicity.

Table 9
Nearby Galaxies of NGC 3842

Name	R.A. (J2000)	Decl. (J2000)	$D(')$ From N3842	PA(deg) From N3842	Notes
N3841	176.00896	19.97189	1.33	0.5	E
N3837	175.98511	19.89458	3.57	202	E
P169975	175.98833	19.95500	1.19	285	S0 CGCG 097090
U06697	175.95446	19.96844	3.26	290	Starburst CGCG 097087
QSO	175.98706	19.94705	1.23	263	at $z = 0.35$

NGC 4104 ($d = 120.0$ Mpc, $1' = 34.9$ kpc, $r_e = 20.0$ kpc, $r_{25} = 44.9$ kpc). This is a dominant galaxy in a small group. Given the shallow *Chandra* observation of this distant galaxy, its 2D spatial features are not clearly visible. Its radial temperature profile shows a cool core (~ 1 keV inside a few kpc) and a temperature peak (~ 1.5 keV) at $r = 20$–40 kpc.

NGC 4125 ($d = 23.9$ Mpc, $1' = 6.9$ kpc, $r_e = 5.9$ kpc, $r_{25} = 20.0$ kpc). This is a flattened elliptical (E6) galaxy. Similar to NGC 3923, the extended hot gas is detected inside the D_{25} ellipse and is elongated along the major axis, but not as flat as the stellar system. It hosts a hot core, as in NGC 3923. The temperature peaks at 0.6 keV at $r = 0.1$ kpc and decreases with increasing r, reaching a minimum (~ 0.3 keV) at the outer boundary where the gas temperature can be measured (~ 30 kpc). It also shows the characteristics of young ellipticals in their X-ray binary luminosity function (Kim & Fabbiano 2010; Zhang et al. 2012).

NGC 4261 ($d = 31.6$ Mpc, $1' = 9.2$ kpc, $r_e = 6.9$ kpc, $r_{25} = 18.7$ kpc). This is a group-dominant elliptical and also an FR-I radio galaxy (3C 270). The bright AGN dominates the X-ray emission. The X-ray jets are detected at the position coincident with the radio jets, and the compressed rims of the X-ray cavities are correlated with radio lobes (Zezas et al. 2005; Worrall et al. 2010; O'Sullivan et al. 2011). The faint diffuse emission from the hot gas is detected inside the D_{25} ellipse. The temperature is constant at ~ 0.7 keV in the inner region ($r = 0.1$–2 kpc), then abruptly increases to 1.3 keV at $r = 5$ kpc, and remains high to the maximum radius (~ 30 kpc).

NGC 4278 ($d = 16.1$ Mpc, $1' = 4.7$ kpc, $r_e = 2.6$ kpc, $r_{25} = 9.5$ kpc). This is one of the gas-poor old elliptical galaxies. With deep *Chandra* observations (560 ks), a population of LMXBs (Brassington et al. 2009; Fabbiano et al. 2010) and their connection to globular clusters (Kim et al. 2009; Fabbiano et al. 2010), and a central LINER activity in conjunction with optical and infrared data (Pellegrini et al. 2012) were extensively investigated. The hot gas is extended out to $r \sim 5$ kpc and the temperature is constant (~ 0.3 keV), but steeply increases to ~ 0.7 keV in the inner 0.3 kpc (see also Pellegrini et al. 2012).

NGC 4291 ($d = 26.2$ Mpc, $1' = 7.6$ kpc, $r_e = 2.0$ kpc, $r_{25} = 7.3$ kpc). Similar to NGC 4342, this is one of a few elliptical galaxies with unusually high BH-bulge mass ratios (see Bogdan et al. 2012b). The hot gas is extended roughly along the major axis, beyond the D_{25} ellipse. It has a hot core with a negative T gradient to the minimum (0.4 keV) at $r \sim 4$ kpc (or 2 r_e), then a positive T gradient to ~ 0.8 keV at $r \sim 10$ kpc. The T map shows that the cooler gas may be extended more to the E than to the W.

NGC 4325 ($d = 110.0$ Mpc, $1' = 32.0$ kpc, $r_e = 10.5$ kpc, $r_{25} = 15.3$ kpc). This is the dominant elliptical galaxy in a small group. The hot gas is extended (beyond the ACIS FOV) and symmetric on a large scale (outside the D_{25} ellipse), the

core region is rather complex with a cool core and cavities (Russell et al. 2007; Lagana et al. 2015). The temperature is about 0.7 keV in the central region, increases to ~ 1.1 keV at $r = 35$ kpc, and then decreases outward. The T map further shows that the cooler gas inside the D_{25} ellipse is elongated along the N-S, roughly following the major axis.

NGC 4342 ($d = 16.5$ Mpc, $1' = 4.8$ kpc, $r_e = 0.5$ kpc, $r_{25} = 3.1$ kpc). This is one of a few elliptical galaxies with unusually high BH-bulge mass ratios (see Bogdan et al. 2012b). In contrast to a nearby massive elliptical NGC 4365, $20'$ away (or 130 kpc in projection), it is optically faint but hot gas rich, hence associated with a large amount of dark matter (Bogdan et al. 2012a). Its $L_{\rm X,GAS}/L_K$ is the highest among local ETGs, making it an extreme opposite to NGC 1316 with the lowest $L_{\rm X,GAS}/L_K$. The SB map shows a head-tail structure with a discontinuity to the NE (just outside the D_{25} ellipse) and a wide extended tail to the SW. The T map shows that the extended tail is filled by cooler (0.6 keV) gas.

NGC 4374 ($d = 18.4$ Mpc, $1' = 5.3$ kpc, $r_e = 5.5$ kpc, $r_{25} = 17.3$ kpc). This is an the extensively studied elliptical galaxy in the Virgo cluster, also known as M84. It is at $17'$ to the SW (PA = 258) from NGC 4406 (M86) and at $89'$ to the NW (PA = 290) from the center of the Virgo cluster, NGC 4486 (M87). The hot gas exhibits many interesting features, including pronounced filaments and cavities in the central region ($r < 10$ kpc), which are associated with the radio jets (Finoguenov et al. 2008) and an extended tail to the SW from the galaxy center in $r = 10$–30 kpc, likely due to the ram pressure (Randall et al. 2008). The T profile shows a hot core with a negative T gradient out to a T minimum (~ 0.6 keV) at $r \sim 1$ kpc, then a positive T gradient to a T maximum (~ 1.5 keV) at $r \sim 30$ kpc. The T maps further show asymmetric, disturbed thermal structures, the cooler gas (~ 0.8 keV) filling the southern part of the D_{25} ellipse and the hotter gas (~ 1.2 keV) filling the extended tail to the SW.

NGC 4382 ($d = 18.5$ Mpc, $1' = 5.4$ kpc, $r_e = 7.4$ kpc, $r_{25} = 19.0$ kpc). This is a young S0 galaxy in the Virgo cluster, also known as M85. It contains a small amount of hot gas for its stellar luminosity (Sansom et al. 2006), and therefore it is often used to study LMXBs (Sivakoff et al. 2003). Within the limited statistics, the relatively cool (~ 0.4 keV) and smooth hot gas does not show a distinct feature.

NGC 4406 ($d = 17.1$ Mpc, $1 = 5.0$ kpc, $r_e = 10.3$ kpc, $r_{25} = 22.2$ kpc). This is an the extensively studied elliptical galaxy in the Virgo cluster, also known as M86. It is at $17'$ to the NE (PA = 78) from NGC 4374 (M84) and at $75'$ to the NW (PA = 296) from the center of the Virgo cluster, NGC 4486 (M87). Its X-ray luminosity is the second highest (M87 is the most luminous) of the Virgo galaxies. The X-ray emission from the extended plume to the NW from the galaxy center is as bright as that of the main body (e.g., Rangarajan et al. 1995). Based on its negative radial velocity (-250 km s^{-1}), it is

moving supersonically in the Virgo cluster with a few other galaxies in the group (e.g., NGC 4438), and the extended plume may be related to ram pressure stripping (e.g., Randall et al. 2008).

NGC 4438 ($d = 18.0$ Mpc, $1' = 5.2$ kpc, $r_e = 5.0$ kpc, $r_{25} = 22.3$ kpc). This is an S0 galaxy in the Virgo cluster and possibly belongs to the M86 group. It is at $23'$ to the E (PA $= 81$) from NGC 4406 (M86) and at $58'$ to the NW (PA $= 310$) from the center of the Virgo cluster, NGC 4486 (M87). In addition to the hot gas in the central region, multiple filaments are visible to $r \sim 10$ kpc to the W and SW, which may be due to the interaction with a nearby galaxy, NGC 4435, which is at $4'.4$ to the NE (Machacek et al. 2004). Also detected are the extended Hα filaments between M86 and NGC 4438, suggesting the interaction between these two galaxies (Kenney et al. 2008).

NGC 4472 ($d = 16.3$ Mpc, $1' = 4.7$ kpc, $r_e = 8.3$ kpc, $r_{25} = 24.2$ kpc). This is an extensively studied hot gas-rich elliptical galaxy in the Virgo cluster, at $4°.4$ to the S from the cluster center, also known as M49. Although it is not at the cluster center, it is the brightest galaxy in the Virgo cluster. There are multiple cavities in the central region ($r < 10$ kpc), the contact discontinuity (a cold front) at ~ 20 kpc to the N and extended tails to the E, as well as longer tails to the SW, which are extended beyond the ACIS FOV. These hot gas features are clearly indicating interactions with the radio jets and ICM in the Virgo cluster (e.g., see Biller et al. 2004 also see Kraft et al. 2011 for *XMM-Newton* data analysis.)

NGC 4477 ($d = 16.5$ Mpc, $1' = 4.8$ kpc, $r_e = 3.5$ kpc, $r_{25} = 9.1$ kpc). This is an SB0 galaxy in the Virgo cluster at $75'.6$ to the N (PA $= 351$) from the center of the Virgo cluster, NGC 4486 (M87). It is also known as Seyfert 2 (Veron-Cetty & Veron 2006), and the X-ray nucleus is detected. The hot gas is relatively cold (0.3–0.4 keV) and confined within the D_{25} ellipse. The SB map shows asymmetry, more extended to the N and W (than to the S and E), and also shows distinct spiral-like features. The *Chandra* observations were primarily obtained for a distant ($z \sim 1$) luminous cluster (Fassbender et al. 2011; Lerchster et al. 2011), XMMU J1230 + 1339, which is at $3'.7$ to the E from NGC 4477.

NGC 4526 ($d = 16.9$ Mpc, $1' = 4.9$ kpc, $r_e = 3.3$ kpc, $r_{25} = 17.8$ kpc). This is an S0 galaxy in the Virgo cluster. It is at $66'$ to the E (PA $= 106°$) from NGC 4472 (M49) and at $4°.8$ to the S (PA $= 170°$) from the center of the Virgo cluster, NGC 4486 (M87). A relatively strong X-ray point source is detected in the center, although it is not a known AGN. The hot gas is relatively weak and cold (0.3 keV) and confined inside 1 r_e.

NGC 4552 ($d = 15.4$ Mpc, $1' = 4.5$ kpc, $r_e = 3.1$ kpc, $r_{25} = 11.4$ kpc). This is a S0 (listed as E0 in RC3) galaxy in the Virgo cluster, at $72'$ to the E from the cluster center, also known as M89. The LINER nucleus source is detected in X-ray (Xu et al. 2005). In contrast to the relaxed old stellar system, the hot gas morphology shows an excellent example of the head-tail structure, likely caused by the relative motion inside the Virgo ICM, as it is falling into the cluster center (Machacek et al. 2006a, 2006b). The cold front on the N has Kelvin–Helmholtz instability structures to the EW direction, and the curved stripped tail is extended to the SE. There are also cavities in the core. See Machacek et al. (2006a) for the discussions on the gas stripping, Machacek et al. (2006b) on the nuclear outflow, and Roediger et al. (2015) on theoretical

modeling in terms of viscosity and KH instability. The T maps clearly show the extended tail filled with ~ 0.6 keV gas. The T profile shows a hot core, with a negative T gradient in the central region, a minimum ($T \sim 0.4$ keV) at 4–5 kpc, and then a positive gradient in the outer region.

NGC 4555 ($d = 91.5$ Mpc, $1' = 26.6$ kpc, $r_e = 13.2$ kpc, $r_{25} = 25.4$ kpc). This is an isolated elliptical, but its relatively high gas temperature ($T_{GAS} \sim 1$ keV) and luminosity ($L_X \sim 10^{41.5}$ erg s^{-1}) may indicate a dominant galaxy in a very poor group with a massive dark halo (O'Sullivan & Ponman 2004). The 2D maps indicate that the hot gas is smooth and relaxed. The T map and profile suggest the presence of a cool core.

NGC 4594 ($d = 9.8$ Mpc, $1' = 2.8$ kpc, $r_e = 3.4$ kpc, $r_{25} = 12.4$ kpc). This is a nearby edge-on S0 galaxy, also known as M104 and Sombrero. Its nucleus and X-ray binaries dominate the entire X-ray emission (Li et al. 2011). After excluding point sources, the temperature map suggests that low-temperature (~ 0.5 keV) gas lies along the disk to the EW of the core. The gas in the perpendicular direction from the disk is slightly hotter (~ 0.7 keV).

NGC 4636 ($d = 14.7$ Mpc, $1' = 4.3$ kpc, $r_e = 6.7$ kpc, $r_{25} = 12.8$ kpc). This is an extensively studied hot gas-rich elliptical galaxy in the Virgo cluster, at $10°$ to the S from the Virgo cluster center and at the northern end of the Virgo South Extension (centered around NGC 4697). The hot gas exhibits spiral-arm like features and cavities on a small scale (<10 kpc), extension to the WSW on an intermediate scale (10–30 kpc), and another extension to the N on a large scale (>50 kpc). The smaller scale features are related to the nuclear activities and radio jets, and the larger scale features are likely sloshing due to the perturbation from nearby galaxies (O'Sullivan et al. 2005; Baldi et al. 2009). As seen in the SB maps, both T profile and map indicate complex thermal structures. The temperature of the hot gas is about 0.5 keV in the central region, increases to ~ 1 keV at ~ 15 kpc, then declines in the outer region. The T maps further show the asymmetric distribution of the inner cooler gas, which is elongated to the N-S direction.

NGC 4649 ($d = 16.8$ Mpc, $1' = 4.9$ kpc, $r_e = 6.2$ kpc, $r_{25} = 18.1$ kpc). This is a giant elliptical galaxy in the Virgo cluster, at $3°.3$ to the E from the cluster center, also known as M60. It hosts a large amount of hot gas, which had been considered as a prototype example of a smooth, relaxed hot halo. However, *Chandra* observations revealed rough asymmetric features both on a small (<3 kpc) scale related to the AGN activity (Paggi et al. 2014) and a large scale (20–30 kpc) related to the bulk motion (Wood et al. 2017). Also detected in the same FOV is a nearby spiral galaxy, NGC 4647, located at $2'.5$ form NGC 4649 in the NW direction. The temperature profile shows a negative gradient inside and a positive gradient outside with a minimum ($T \sim 0.8$ keV) at $r \sim 1$ kpc. A hot core in the center has been discussed in Pellegrini et al. (2012) and Paggi et al. (2014). The temperature map further indicates that the cooler gas (0.8–0.9 keV) extends preferentially to the NE and SW directions, the same directions where two extended wings are visible, while the gas in the other directions (NW and SE) is hotter (1–1.2 keV). Wood et al. (2017) suggested that the two wings might be caused by the Kelvin–Helmholtz instability while the galaxy is infalling toward the center of the Virgo cluster. However, the cooler gas extended from the center may imply that the extended wings may also be related to the AGN outflows.

Table 10
Nearby Galaxies of 5171

Name	R.A.	Decl.	D (′)	PA(deg) From N5171	From N5171
	(J2000)	(J2000)			
N5176	202.35399	11.78148	2.′9	17	
N5177	202.35108	11.79703	3.′8	10	
N5179	202.37869	11.74583	2.′4	74	
SDSS	J132920.65+114424.1		0.′4	326	
SDSS	J132928.18+114625.2		2.′8	35	

NGC 4782 ($d = 60.0$ Mpc, $1' = 17.5$ kpc, $r_e = 4.4$ kpc, $r_{25} = 15.5$ kpc). This is in a close pair VV201 with NGC 4783, also known as the Dumbbell galaxies. NGC 4782 is also an FR-I radio galaxy (3C 278). The hot ISM (~ 0.5 keV) in both galaxies is embedded inside the hotter (~ 1.4 keV) ICM (see Machacek et al. 2007). The hot gas is highly disturbed. The hot gas in NGC 4782 exhibits a cavity and X-ray knots that are related to the radio jets, and the hot gas of NGC 4783 exhibits a head-tail structure (a cold front and an extended tail) caused by the ram pressure as it is apparently moving to the E.

NGC 5044 ($d = 31.2$ Mpc, $1' = 9.1$ kpc, $r_e = 3.9$ kpc, $r_{25} = 13.4$ kpc). This is a dominant galaxy in the X-ray brightest group in the sky. Its extended hot halo has been extensively studied from the early X-ray missions. The deep *Chandra* observations show that the hot gas is sloshing with fronts visible in surface brightness and abundance, temperature maps with many small cavities (David et al. 2009, 2011, 2017). Also shown in *XMM-Newton* data is a large-scale sloshing (O'Sullivan et al. 2014)

NGC 5129 ($d = 103.0$ Mpc, $1' = 30.0$ kpc, $r_e = 14.3$ kpc, $r_{25} = 25.4$ kpc). This is the dominant galaxy in a small group (Eckmiller et al. 2011, see also Bharadwaj et al. 2014).

The hot gas has a cool core with a positive temperature gradient in the inner region to a peak (~ 1 keV) at $r \sim 20$ kpc and a negative gradient in the outer region to the FOV limit ($r_{max} \sim 200$ kpc).

NGC 5171 ($d = 100.0$ Mpc, $1' = 29.1$ kpc, $r_e = 12.4$ kpc, $r_{25} = 15.9$ kpc). This is the dominant galaxy in a small group with multiple roughly equal sized ellipticals. The hot ISM ($L_X \sim$ a few $\times 10^{40}$ erg s^{-1}) directly associated with NGC 5171 is confined within r_e with $T \sim 1$ keV and is roughly symmetric inside r_e. Interestingly, there is a large amount (($L_X \sim$ a few $\times 10^{41}$ erg s^{-1}) of hotter gas (1.2–1.3 keV) filling gaps among group galaxies (see also Osmond et al. 2004), mostly to the N and the E from NGC 5171. Also detected in a single *Chandra* observation are three large galaxies (NGC 5179, NGC 5176, and NGC 5177) and two small galaxies (SDSS J132920.65 +114424.1 and SDSS J132928.18+114625.2). The temperatures of their hot ISM are in the range of 0.3–0.6 keV (see also Jeltema et al. 2008). See Table 10 for the list of nearby galaxies.

NGC 5813 ($d = 32.2$ Mpc, $1' = 9.4$ kpc, $r_e = 8.3$ kpc, $r_{25} = 19.5$ kpc). This is the dominant galaxy in a small group. The hot gas morphology exhibits three sets of nested coaligned cavities and shocks (Randall et al. 2011, 2015). The temperature map shows cooler uplifted material along the line of cavities.

NGC 5846 ($d = 24.9$ Mpc, $1' = 7.2$ kpc, $r_e = 7.2$ kpc, $r_{25} = 14.7$ kpc). This is the dominant galaxy in a small group. The hot gas morphology exhibits small-scale cavities

associated with radio jets in the central region and spiral-like tails and multiple cold fronts on a large scale that may be caused by sloshing due to a nearby galaxy NGC 5850 (Machacek et al. 2011; Gastaldello et al. 2013; Paggi et al. 2017).

N5866 ($d = 15.4$ Mpc, $1' = 4.5$ kpc, $r_e = 2.8$ kpc, $r_{25} = 10.4$ kpc). This is a nearby edge-on S0 galaxy, hosting a LINER nucleus. It could be M102, which has not been identified unambiguously. Li et al. (2009) investigated the weak diffuse hot gas that is extended as far as 3.5 kpc away from the galactic plane. The faint spiral-like filament to the S lying outside the D25 ellipse may be interesting, but needs to be confirmed by deeper observations.

NGC 6107 ($d = 127.9$ Mpc, $1' = 37.2$ kpc, $r_e = 16.3$ kpc, $r_{25} = 15.8$ kpc). This is the dominant galaxy in a small group. The hot ISM (~ 1 keV) inside the D$_{25}$ ellipse shows an elongated structure in the SE-NW direction (roughly along the minor axis), which is surrounded by the hotter (~ 1.5 keV) gas. The large-scale *ROSAT* observation (Feretti et al. 1995) showed that the hotter IGM extends to the entire regions connecting NGC 6107 and NGC 6109 (at 7.′5 to the NE from NGC 6107). It is also known as a radio galaxy, B2 1615 + 35, with an SE-NW radio extension (Feretti et al. 1995; Condon et al. 2002), which is interestingly along the same direction with the inner hot gas feature.

NGC 6338 ($d = 123.0$ Mpc, $1' = 35.8$ kpc, $r_e = 17.1$ kpc, $r_{25} = 27.1$ kpc). This is the dominant galaxy in a small group, possibly merging with PGC 59943 (or MCG +10-24-117) at 1.2 arcmin to the N. Both galaxies have stripped tails and multiple cavities (Pandge et al. 2012). The tail of PGC 59943 is stretched to the N, indicating that this galaxy is moving to the S. In this ACIS-I image, the chip gaps are visible in raw binned images and some spectral maps, mostly significant in CB (because a spatial bin was determined in a region with similar counts/area), but least so in WB. The T profile and map show the presence of a cool core inside r_e.

NGC 6482 ($d = 58.4$ Mpc, $1' = 17.0$ kpc, $r_e = 6.3$ kpc, $r_{25} = 16.9$ kpc). This is an isolated elliptical or a fossil group galaxy with a relatively relaxed hot gas morphology (Khosroshahi et al. 2004; Buote 2017). In contrast to typical relaxed systems, the hot gas is hotter in the inner region than in the outer region, with the temperature monotonically decreasing outward from 0.9 keV at the center to 0.5 keV at 50 kpc. The Suzaku data suggest a hint that the temperature may increase slightly (to 0.65 keV) at the outer region ~ 100 kpc (Buote 2017). All spectral maps show roughly circularly symmetric distribution, except in the inner 10 kpc region, where the hotter gas is slightly elongated in the SE-NW direction (roughly along the minor axis direction), more pronounced to the SE.

NGC 6861 ($d = 28.0$ Mpc, $1' = 8.2$ kpc, $r_e = 3.1$ kpc, $r_{25} = 11.5$ kpc). This is one of the two dominant galaxies (with NGC 6868 at 26′ to the E) in the Telescopium galaxy group. While NGC 6861 is slightly less luminous (by a factor of 1.4) than NGC 6868, its velocity dispersion is higher (by a factor or 1.7). The hot gas morphology indicates that the two galaxies (or two subgroups) are possibly merging. The hot gas in NGC 6861 has bifurcated tails trailing NGC 6861 at ~ 40 kpc to the W and NW, likely caused by the subgroup merger (Machacek et al. 2010).

NGC 6868 ($d = 26.8$ Mpc, $1' = 7.8$ kpc, $r_e = 3.9$ kpc, $r_{25} = 13.8$ kpc). This is one of the two dominant galaxies in

the Telescopium galaxy group, possibly merging with NGC 6861 at $26'$ to the W. There is a cold front at $\sim$23 kpc to the N, likely caused by sloshing due to the merger (Machacek et al. 2010). The T maps further show an asymmetry in the hot gas morphology with slightly colder gas ($\sim$0.6 keV) forming a shell-like feature that is more pronounced to the NE than to the S on the scale of the D_{25} ellipse.

NGC 7618 ($d = 74.0$ Mpc, $1' = 21.5$ kpc, $r_e = 7.7$ kpc, $r_{25} = 12.9$ kpc). This is the dominant galaxy in a small group, showing an excellent example of the pronounced spiral-like features caused by sloshing and the associated structures caused by turbulent instability. It is likely merging with UGC 12491 (PGC 71014), at $14'$ to the NW from NGC 7618 (Kraft et al. 2006; Roediger et al. 2012). The T maps clearly show the curved, extended tail filled with 0.7–0.8 keV gas, which is surrounded by $\sim$1.2 keV hotter ambient gas. Note that the tail is more pronounced in the T map than in the SB map. The tail is clearly visible in the EM and projected entropy maps, but almost invisible in the projected pressure map, possibly indicating pressure balance with the ambient gas.

N7619 ($d = 53.0$ Mpc, $1' = 15.4$ kpc, $r_e = 8.8$ kpc, $r_{25} = 19.4$ kpc). This is the dominant E galaxy in the Pegasus I group. It has a cold front to the NE and extended tails to the SW. The X-ray tail is metal-enriched, suggesting that the hot gas is originated from the galaxy (Kim et al. 2008). A nearby galaxy, NGC 7626, at $7'$ to the E is possibly interacting with NGC 7619.

NGC 7626 ($d = 56.0$ Mpc, $1' = 16.3$ kpc, $r_e = 12.0$ kpc, $r_{25} = 21.4$ kpc). This is an E galaxy in the Pegasus I group at $7'$ to the E from the NGC 7619. The surface brightness and temperature maps suggest that it is possibly merging with NGC 7619 (Randall et al. 2009).

ORCID iDs

Dong-Woo Kim ⓘ https://orcid.org/0000-0002-7386-944X
Douglas Burke ⓘ https://orcid.org/0000-0003-4428-7835
Raffaele D'Abrusco ⓘ https://orcid.org/0000-0003-3073-0605
Giuseppina Fabbiano ⓘ https://orcid.org/0000-0002-3554-3318
Michael McCollough ⓘ https://orcid.org/0000-0002-8384-3374
Ewan O'Sullivan ⓘ https://orcid.org/0000-0002-5671-6900
Alessandro Paggi ⓘ https://orcid.org/0000-0002-5646-2410

References

Alabi, A. B., Forbes, D. A., & Romanowsky, A. J. 2016, MNRAS, 460, 3838
Baldi, A., Forman, W., Jones, C., et al. 2009, ApJ, 707, 1034
Bharadwaj, V., Reiprich, T. H., Schellenberger, G., et al. 2014, A&A, 572, A46
Bilek, M., Cuillandre, J.-C., Gwyn, S., et al. 2016, A&A, 588, 77
Biller, B. A., Jones, C., Forman, W. R., Kraft, R., & Ensslin, T. 2004, ApJ, 613, 238
Blanton, E. L., Sarazin, C. L., & Irwin, J. A. 2001, ApJ, 552, 106
Bogdan, A., Forman, W. R., Kraft, R. P., et al. 2012a, ApJ, 755, 25
Bogdan, A., Forman, W. R., Zhuravleva, I., et al. 2012b, ApJ, 753, 140
Bogdan, A., van Weeren, R. J., Kraft, R. P., et al. 2014, ApJL, 782, L19
Boroson, B., Kim, D.-W., & Fabbiano, G. 2011, ApJ, 729, 12
Brassington, N. J., Fabbiano, G., Blake, S., et al. 2010, ApJ, 725, 1805
Brassington, N. J., Fabbiano, G., Kim, D. W., et al. 2008, ApJS, 179, 142
Brassington, N. J., Fabbiano, G., Kim, D.-W., et al. 2009, ApJS, 181, 605
Buote, D. A. 2017, ApJ, 834, 164
Buote, D. A., Jeltema, T. E., Canizares, C. R., & Garmire, G. P. 2002, ApJ, 577, 183
Cappellari, M., & Copin, Y. 2003, MNRAS, 342, 345
Cappellari, M., Emsellem, E., Krajnovi'c, D., et al. 2011, MNRAS, 413, 813
Choi, E., Ostriker, J. P., Naab, T., et al. 2017, ApJ, 844, 31
Ciotti, L., Pellegrini, S., Negri, A., et al. 2017, ApJ, 835, 15
Condon, J. J., Cotton, W. D., & Broderick, J. J. 2002, AJ, 124, 675
Crook, A. C., Huchra, J. P., Martimbeau, N., et al. 2007, ApJ, 655, 790
D'Abrusco, R., Fabbiano, G., Mineo, S., et al. 2014, ApJ, 783, 18
David, L. P., Jones, C., Forman, W., et al. 2009, ApJ, 705, 624
David, L. P., O'Sullivan, E., Jones, C., et al. 2011, ApJ, 728, 162
David, L. P., Vrtilek, J., O'Sullivan, E., et al. 2017, ApJ, 842, 84
de Plaa, J., Zhuravleva, I., Werner, N., et al. 2012, A&A, 539, A34
de Vaucouleurs, G., de Vaucouleurs, A., Corwin, H. G., et al. 1991, Third Reference Catalog of Bright Galaxies (RC3) (New York: Springer)
Deason, A. J., Belokurov, V., Evans, N. W., & McCarthy, I. G. 2012, ApJ, 748, 2
Dickey, J. M., & Lockman, F. J. 1990, ARA&A, 28, 215
Diehl, S., & Statler, T. S. 2006, MNRAS, 368, 497
Diehl, S., & Statler, T. S. 2007, ApJ, 668, 150
Diehl, S., & Statler, T. S. 2008a, ApJ, 680, 897
Diehl, S., & Statler, T. S. 2008b, ApJ, 687, 986
Dong, R., Rasmussen, J., & Mulchaey, J. S. 2010, ApJ, 712, 883
Eckmiller, H. J., Hudson, D. S., & Reiprich, T. H. 2011, A&A, 535A, 105
Ekers, R. D., Gross, W. M., Wellington, K. J., et al. 1983, A&A, 127, 361
Fabbiano, G., Elvis, M., Markoff, S., et al. 2003, ApJ, 588, 175
Fabbiano, G., Brassington, N. J., Lentati, L., et al. 2010, ApJ, 725, 1824
Fassbender, R., Böhringer, H., Santos, J. S., et al. 2011, A&A, 527A, 78
Feretti, L., Fanti, R., Parma, P., et al. 1995, A&A, 298, 699
Finoguenov, A., Ruszkowski, M., Jones, C., et al. 2008, ApJ, 686, 911
Flohic, H. M. L. G., Eracleous, M., Chartas, G., et al. 2006, ApJ, 647, 140
Forbes, D. A., Alabi, A., Romanowsky, A. J., et al. 2017, MNRAS, 464, 26
Garcia, A. M. 1993, A&AS, 100, 47
Gastaldello, F., Di Gesu, L., Ghizzardi, S., et al. 2013, ApJ, 770, 56
Giacintucci, S., O'Sullivan, E., Clarke, T. E., et al. 2012, ApJ, 755, 172
Giacintucci, S., O'Sullivan, E., Vrtilek, J., et al. 2011, ApJ, 732, 95
Goulding, A. D., Greene, J. E., Ma, C.-P., et al. 2016, ApJ, 826, 167
Grevesse, N., & Sauval, A. J. 1998, SSRv, 85, 161
Hardcastle, M. J., Worrall, D. M., Birkinshaw, M., et al. 2002, MNRAS, 334, 182
Hernández-García, L., González-Martín, O., Márquez, I., et al. 2013, A&A, 556, 47
Humphrey, P. J., & Buote, D. A. 2006, ApJ, 639, 136
Humphrey, P. J., Buote, D. A., Canizares, C. R., Fabian, A. C., & Miller, J. M. 2011, ApJ, 729, 53
Humphrey, P. J., Buote, D. A, Brighenti, F., Gebhardt, K., & Mathews, W. G. 2013, MNRAS, 430, 1516
Jeltema, T., Binder, B., & Mulchaey, J. S. 2008, ApJ, 679, 1162
Jetha, N. N., Hardcastle, M. J., Babul, A., et al. 2008, MNRAS, 384, 1344
Kawaharada, M., Makishima, K., Kitaguchi, T., et al. 2009, ApJ, 691, 971
Kenney, J. D. P., Tal, T., Crowl, H. H., Feldmeier, J., & Jacoby, G. H. 2008, ApJL, 687, L69
Khosroshahi, H. G., Jones, L. R., & Ponman, T. J. 2004, MNRAS, 349, 1240
Kim, D.-W., Anderson, C., Burke, D., et al. 2018, ApJ, 853, 129
Kim, D.-W., & Fabbiano, G. 2003, ApJ, 586, 826
Kim, D. W., & Fabbiano, G. 2010, ApJ, 721, 1523
Kim, D.-W., & Fabbiano, G. 2013, ApJ, 776, 116
Kim, D.-W., & Fabbiano, G. 2015, ApJ, 812, 127
Kim, D.-W., Fabbiano, G., Brassington, N. J., et al. 2009, ApJ, 703, 829
Kim, D.-W., Fabbiano, G., & Pipino, A. 2012, ApJ, 715, 38
Kim, D.-W., Kim, E., Fabbiano, G., et al. 2008, ApJ, 688, 931
Kim, D.-W., & Pellegrini, S. 2012, ASSL, 378
Kraft, R. P., Forman, W. R., Churazov, E., et al. 2004, ApJ, 601, 221
Kraft, R. P., Forman, W. R., Jones, C., et al. 2011, ApJ, 727, 41
Kraft, R. P., Jones, C., Nulsen, P. E. J., et al. 2006, ApJ, 640, 762
Kundu, A., Maccarone, T. J., & Zepf, S. E. 2002, ApJL, 574, L5
Lagana, T. F., Lovisari, L., Martins, L., et al. 2015, A&A, 573A, 66
Laing, R. A., Guidetti, D., Bridle, A. H., et al. 2011, MNRAS, 417, 2789
Lakhchaura, K., Werner, N., Sun, M., et al. 2018, MNRAS, 481, 4472
Lerchster, M., Seitz, S., Brimioulle, F., et al. 2011, MNRAS, 411, 2667
Li, J.-T., Wang, Q. D., Li, Z., et al. 2009, ApJ, 706, 693
Li, Z., Jones, C., Forman, W. R., et al. 2011, ApJ, 730, 84
Lin, D., Irwin, J. A., Wong, K.-W., et al. 2015a, ApJ, 808, 19
Lin, D., Irwin, J. A., Wong, K.-W., et al. 2015b, ApJ, 808, 20
Lovisari, L., Reiprich, T. H., & Schellenberger, G. 2015, A&A, 573A, 118
Machacek, M., Jones, C., Forman, W. R., & Nulsen, P. 2006a, ApJ, 644, 155
Machacek, M., Nulsen, P. E. J., Jones, C., & Forman, W. R. 2006b, ApJ, 648, 947

Machacek, M. E., Dosaj, A., Forman, W., et al. 2005, ApJ, 621, 663
Machacek, M. E., Jerius, D., Kraft, R., et al. 2011, ApJ, 743, 15
Machacek, M. E., Jones, C., & Forman, W. R. 2004, ApJ, 610, 183
Machacek, M. E., Kraft, R. P., Jones, C., et al. 2007, ApJ, 664, 804
Machacek, M. E., O'Sullivan, E., Randall, S. W., et al. 2010, ApJ, 711, 1316
Markevitch, M., Bautz, M. W., Biller, B., et al. 2003, ApJ, 583, 70
Mazzei, P., Marino, A., & Rampazzo, R. 2014, ApJ, 782, 53
Negri, A., Posacki, S., Pellegrini, S., et al. 2014, MNRAS, 445, 1351
O'Sullivan, E., David, L. P., & Vrtilek, J. M. 2014, MNRAS, 437, 730
O'Sullivan, E., Forbes, D. A., & Ponman, T. J. 2001, MNRAS, 328, 461
O'Sullivan, E., & Ponman, T. J. 2004, MNRAS, 354, 935
O'Sullivan, E., Ponman, T. J., & Collins, R. S. 2003, MNRAS, 340, 1375
O'Sullivan, E., Ponman, T. J., Kolokythas, K., et al. 2017, MNRAS, 472, 1482
O'Sullivan, E., Vrtilek, J. M., Harris, D. E., et al. 2007, ApJ, 658, 299
O'Sullivan, E., Vrtilek, J. M., & Kempner, J. C. 2005, ApJL, 624, L77
O'Sullivan, E., Worrall, D. M., Birkinshaw, M., et al. 2011, MNRAS, 416, 2916
Osmond, J. P. F., Ponman, T. J., & Finoguenov, A. 2004, MNRAS, 355, 11
Paggi, A., Fabbiano, G., Kim, D.-W., et al. 2014, ApJ, 787, 134
Paggi, A., Kim, D.-W., Anderson, A., et al. 2017, ApJ, 844, 5
Panagoulia, E. K., Fabian, A. C., & Sanders, J. S. 2014, MNRAS, 438, 2341
Pandge, M. B., Vagshette, N. D., David, L. P., et al. 2012, MNRAS, 421, 808
Paolillo, M., Fabbiano, G., Peres, G., & Kim, D.-W. 2002, ApJ, 565, 883
Pellegrini, S., Venturi, T., Comastri, A., et al. 2003, ApJ, 585, 677
Pellegrini, S., Wang, J., Fabbiano, G., et al. 2012, ApJ, 758, 94
Randall, S., Nulsen, P., Forman, W. R., et al. 2008, ApJ, 688, 208
Randall, S. W., Forman, W. R., Giacintucci, S., et al. 2011, ApJ, 726, 86
Randall, S. W., Jones, C., Kraft, R., Forman, W. R., & O'Sullivan, E. 2009, ApJ, 696, 1431
Randall, S. W., Nulsen, P. E. J., Jones, C., et al. 2015, ApJ, 805, 24
Rangarajan, F. V. N., White, D. A., Ebeling, H., & Fabian, A. C. 1995, MNRAS, 277, 1047
Rasmussen, J., Bai, X.-N., Mulchaey, J. S., et al. 2012, ApJ, 747, 31
Rasmussen, J., Ponman, T. J., & Mulchaey, J. S. 2006, MNRAS, 370, 453
Roediger, E., Kraft, R. P., Machacek, M. E., et al. 2012, ApJ, 754, 147
Roediger, E., Kraft, R. P., Nulsen, P. E. J., et al. 2015, ApJ, 806, 104
Russell, P. A., Ponman, T. J., & Sanderson, A. J. R. 2007, MNRAS, 378, 1217
Sanders, J. S. 2006, MNRAS, 371, 829
Sansom, A. E., O'Sullivan, E., Forbes, D. A., et al. 2006, MNRAS, 370, 1541

Sarazin, C. L., Kundu, A., Irwin, J. A., et al. 2003, ApJ, 595, 743
Scharf, C. A., Zurek, D. R., & Bureau, M. 2005, ApJ, 633, 154
Schellenberger, G., Vrtilek, J. M., David, L., et al. 2017, ApJ, 845, 84
Schweizer, F. 1980, ApJ, 237, 303
Shin, J., Woo, J.-H., & Mulchaey, J. S. 2016, ApJS, 227, 31
Sivakoff, G. R., Sarazin, C. L., & Carlin, J. L. 2004, ApJ, 617, 262
Sivakoff, G. R., Sarazin, C. L., & Irwin, J. A. 2003, ApJ, 599, 218
Smith, R. M., Martínez, V. J., Fernández-Soto, A., et al. 2008, ApJ, 679, 420
Statler, T. S., & McNamara, B. R. 2002, ApJ, 581, 1032
Su, Y., Gu, L., White, R., & Irwin, J. 2014, ApJ, 786, 152
Su, Y., Kraft, R. P., Nulsen, P. E. J., et al. 2017a, ApJ, 835, 19
Su, Y., Nulsen, P. E. J., Kraft, R. P., et al. 2017b, ApJ, 851, 69
Sun, M., Forman, W., Vikhlinin, A., et al. 2003, ApJ, 598, 250
Sun, M., & Vikhlinin, A. 2005, ApJ, 621, 718
Sun, M., Vikhlinin, A., Forman, W., et al. 2005, ApJ, 619, 169
Sun, M., Voit, G. M., Donahue, M., et al. 2009, ApJ, 693, 1142
Thomas, J., Ma, C.-P., McConnell, N. J., et al. 2016, Natur, 532, 340
Tonry, J. L., Dressler, A., Blakeslee, J. P., et al. 2001, ApJ, 546, 681
Trinchieri, G., Breitschwerdt, D., Pietsch, W., et al. 2007, A&A, 463, 153
Trinchieri, G., Pellegrini, S., Fabbiano, G., et al. 2008, ApJ, 688, 1000
Tully, R. B., Courtois, H. M., Dolphin, A. E., et al. 2013, AJ, 146, 86
Veron-Cetty, M.-P., & Veron, P. 2006, A&A, 455, 773
Vikhlinin, A. 2006, ApJ, 640, 710
Vikhlinin, A., Markevitch, M., Murray, S. S., et al. 2005, ApJ, 628, 655
Voit, G. M., Ma, C. P., Greene, J., et al. 2018, ApJ, 853, 78
von Benda-Beckmann, A. M., D'Onghia, E., Gottlöber, S., et al. 2008, MNRAS, 386, 2345
Vrtilek, S. D., & Boroson, B. S. 2013, MNRAS, 428, 3693
Werner, N., Allen, S. W., & Simionescu, A. 2012, MNRAS, 425, 2731
Wong, K.-W., Irwin, J. A., Shcherbakov, R. V., et al. 2014, ApJ, 780, 9
Wood, R. A., Jones, C., Machacek, M. E., et al. 2017, ApJ, 847, 79
Worrall, D. M., Birkinshaw, M., & Hardcastle, M. J. 2003, MNRAS, 343, L73
Worrall, D. M., Birkinshaw, M., Laing, R. A., et al. 2007, MNRAS, 380, 2
Worrall, Birkinshaw, M., O'Sullivan, E., et al. 2010, MNRAS, 408, 701
Xu, Y., Xu, H., Zhang, Z., et al. 2005, ApJ, 631, 809
Zezas, A., Birkinshaw, M., Worrall, D. M., Peters, A., & Fabbiano, G. 2005, ApJ, 627, 711
Zhang, Z., Gilfanov, M., & Bogdan, A. 2012, A&A, 546, A36